Phase separation in lipid-based nanoparticles: exploring the nano-bio interface

Papadopoulou, P.

CHAPTER 2

Phase-separated liposomes hijack endogenous lipoprotein transport and metabolism pathways to target subsets of endothelial cells *in vivo*

This chapter was published as a research article:

Gabriela Arias-Alpizar[#], **Panagiota Papadopoulou[#]**, Xabier Rios, Krishna Reddy Pulagam, Mohammad-Amin Moradi, Roy Pattipeiluhu, Jeroen Bussmann, Nico Sommerdijk, Jordi Llop, Alexander Kros[*], Frederick Campbell[*]. Advanced Healthcare Materials 2022, 12(10), e2202709.

# denotes equal contribution

Abstract | Plasma lipid transport and metabolism is essential to ensure correct cellular function throughout the body. Dynamically regulated in time and space, the well characterized mechanisms underpinning plasma lipid transport and metabolism offer an enticing, but as yet underexplored, rationale to design synthetic lipid nanoparticles with inherent cell/tissue selectivity. Herein, we describe a systemically administered liposome formulation, composed of just two lipids, that is capable of hijacking a triglyceride lipase-mediated lipid transport pathway, resulting in liposome recognition and uptake within specific endothelial cell subsets. In the absence of targeting ligands, liposome-lipase interactions are mediated by a unique, phase-separated ('parachute') liposome morphology. Within the embryonic zebrafish, selective liposome accumulation is observed at the developing blood-brain-barrier. In mice, extensive liposome accumulation within the liver and spleen – which is reduced but not eliminated following small molecule lipase inhibition – supports a role for endothelial lipase, but highlights these liposomes are also subject to significant 'off-target' by reticuloendothelial system organs. Overall, these compositionally simplistic liposomes offer new insights into the discovery and design of lipid-based nanoparticles that can exploit endogenous lipid transport and metabolism pathways to achieve cell selective targeting *in vivo*.

2.1 Introduction

All cells rely on plasma lipid transport to maintain a correct intracellular balance of essential and non-essential fatty acids. This requires the dynamic regulation of the secretion, transport, and metabolism of water-insoluble fats throughout the body. Often packaged, secreted, and transported as nanometer-sized, solid lipid particles (*i.e.*, lipoproteins), many of the biological mechanisms underpinning endogenous plasma lipid transport and metabolism are now well understood.[1]

Despite compositional and structural similarities of lipoproteins and synthetic lipid-based nanoparticles however, there are currently only a few examples of nanoparticles that explicitly hijack endogenous lipid transport mechanisms to achieve target cell specificity. One notable example, however, is Onpattro® – a clinically approved lipid nanoparticle (LNP)-RNAi therapy used to treat polyneuropathies resulting from transthyretin-mediated amyloidosis (hATTR). In this case, selective recognition and uptake within target hepatocytes relies on the adsorption of soluble apolipoprotein E (apoE) to the surface of circulating LNPs. This, in turn, guides Onpattro® to low density lipoprotein receptors (LDLr) that are heavily expressed on the sinusoidal surface of hepatocytes.[2,3] This clinically relevant lipid nanoparticle formulation highlights the enticing, but largely unexplored,[4,5] potential of exploiting endogenous lipid transport to guide nanoparticles to specific tissues and cells within the body.

The three main plasma lipid transport forms are free fatty acids (FFAs), triglycerides (TGs) and cholesteryl esters (CEs).[1] FFAs are generally transported as a complex with serum albumin, whereas TGs and CEs are transported within the core of plasma lipoproteins – solid lipid particles surrounded by a lipid monolayer rich in phospholipids – and stabilized by apolipoprotein(s). The five major classes of lipoproteins are chylomicrons (secreted by intestine, *size*: 100 – 1000 nm); very-low density lipoproteins (VLDLs, secreted by liver, *size*: 50 – 200 nm); intermediate and low density lipoproteins (IDLs and LDLs, lipoprotein metabolites enriched in cholesterol, and, at high levels, associated with atherogenic disorders [6,7] *size*: 20 – 50 nm); and high density lipoproteins (HDLs, involved in reverse cholesterol transport,[8] size 8 – 12 nm). In the case of VLDL and chylomicrons, a single, surface-

bound apolipoprotein B – apoB100 or apoB48 respectively – stabilizes each secreted lipoprotein. HDLs, in contrast, are stabilized by apolipoprotein A-I (apoAI).[9,10] Once secreted into the bloodstream, soluble and exchangeable apolipoproteins (*e.g.*, apoA, C, D and E) recognize and bind to the surface of a circulating lipoprotein. These apolipoproteins guide lipoproteins to specific targets within the body. For example, apoE is a ligand for LDLr, promoting uptake primarily in hepatocytes,[11] lipoprotein-bound apoC2 functions as an obligatory cofactor of lipoprotein lipase (LPL),[12,13] whereas apoA1 binds a wide range of cognate receptors and enzymes including LDLr,[14] scavenger receptor B-1 (SRB-1),[15–17] ATP-binding cassette transporters A1 (ABCA1) and G1 (ABCG1),[18–20] and endothelial lipase (EL).[21,22]

Following transport, lipoproteins are generally metabolized to release free fatty acids that are then taken up locally by cells. TG lipases are key extracellular, hydrolytic enzymes that regulate lipid metabolism throughout the body. The three main members of the TG lipase family are LPL,[23] hepatic lipase (HL),[24] and EL[21,25] (encoded by the human genes *LPL*, *LIPC,* and *LIPG* respectively). All three share significant structural homology, including a conserved catalytic triad of amino acids (serine, aspartate and histidine), as well as conserved heparin and lipoprotein binding domains.[21,25] LPL is predominantly synthesized in adipose tissue, heart and skeletal muscle; HL in hepatocytes; and EL in vascular endothelial cells.[21] Once expressed, TG lipases are secreted and actively transported (in the case of LPL and HL) to the local endothelium where they anchor to heparan sulfate proteoglycans (HSPG) *via* electrostatic interactions.[22] As hydrolytic enzymes, LPL primarily hydrolyzes TGs,[26] HL – TGs and phospholipids,[24,27] and EL – phospholipids.[21] Substrate specificity is determined by sequence variation in the lid region of each enzyme.[21,28,29] However, whereas LPL and HL metabolize fats primarily derived from VLDL and chylomicrons, the principle function of EL is the regulation of HDL metabolism *via* interactions with apoA-1.[21,30–33] In addition, all three TG lipase family members are capable of internalizing lipoproteins *via* proteoglycan- or receptor-mediated pathways in a non-enzymatic fashion.[22,34,35]

Herein, we describe a systemically administered liposome formulation, composed of just two lipids, that preferentially targets a specific subset of endothelial cells *in vivo*. Most notably, these liposomes accumulate at the brain endothelium of an

embryonic zebrafish. Mechanistically, we show that target selectivity is linked to the ability of these liposomes to interact with endogenous (endothelial) lipase, although whether cell selectivity arises as a result of direct (*e.g.*, non-enzymatic lipase-mediated recognition and uptake) or indirect (*i.e.,* lipase mediated metabolism prior to cellular uptake) lipase engagement is not yet clear. With no additional 'targeting' functionality, lipase-liposome interactions are mediated through a unique, phase-separated ("parachute") liposome morphology, onto the surface of which preferentially adsorb apolipoproteins A1, A4 and E. Within 6-8 week old mice, liposomes predominantly accumulate within the liver and spleen. While in the liver, we show liposome accumulation is in part mediated by lipase interaction, these observations ultimately reaffirm that the capacity of these RES organs to clear nanoparticles from circulation is both proficient and mechanistically multipronged.

2.2 Results

PAP3 liposomes accumulate at the brain endothelium of embryonic zebrafish

Zebrafish embryos are convenient, accurate and cost effective animals to study the behavior and pharmacokinetics of nanoparticles *in vivo*,[36,37] to assess and predict key nanoparticle-liver interactions within higher vertebrates and to identify endogenous biological pathways underpinning nanoparticle fate *in vivo*.[38–40] From a preliminary screen of intravenously (*i.v.*) administered liposomes, we unexpectedly observed selective accumulation of a liposomal formulation, PAP3, within the head region of a ~78 hours post fertilization (hpf) zebrafish embryo (**Figure 1a, b)**. PAP3 liposomes (size: ~120 nm) were composed of an equimolar mixture of just two lipids: a novel synthetic lipid, 2-hydroxy-3-oleamidopropyl oleate (DOaG), and the naturally occurring, 1,2-distearyl-*sn*-glycero-3-phosphocholine (DSPC) (**Figure 1c**). These liposomes contained no additional targeting functionality. Looking closely within the head region of the zebrafish embryo, PAP3 liposomes clearly accumulated within some (*e.g.*, mesencephalic vein (MsV), mesencephalic artery (MsA), middle mesencephalic central artery (MMCtA), middle cerebral vein (MCeV), primordial

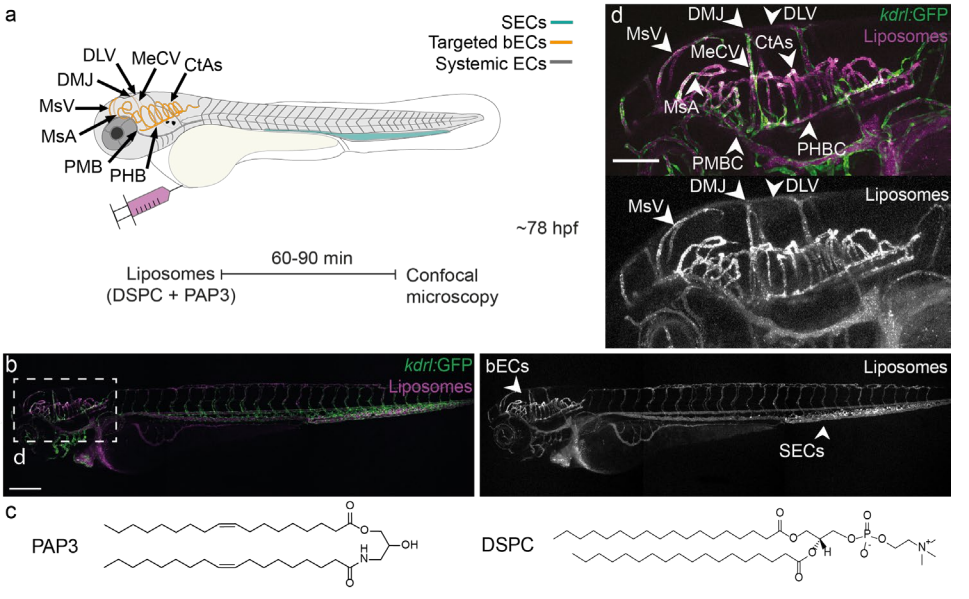

Figure 1. Biodistribution of PAP3 liposomes within zebrafish embryos (78 hpf). a) Schematic zebrafish larvae in lateral (whole body) view, showing the site of microinjection and key cranial vessels. Fluorescently labeled liposomes are imaged with confocal microscopy after 60-90 min. The vasculature as follows, liposome targeted bECs in yellow and systemic endothelium in dark gray, scavenging endothelial cells (SECs) in cyan, at ~78 hours post fertilization (hpf). **b)** Biodistribution (10x magnification, lateral view) of PAP3 liposomes within a Tg(kdrl:GPF) zebrafish embryo at 1.5 hours post injection (hpi). **c)** Molecular structure of lipids used in equimolar mixture for the formulation of PAP3 liposomes, DOaG and DSPC. **d)** Zoom of the cranial region in lateral view. bECs = brain endothelial cells; CtAs = central arteries; DLV = dorsal longitudinal vein; DMJ = dorsal midline junction; MCeV = middle cerebral vein; MsA = mesencephalic artery; MsV = mesencephalic vein; PMBC = primordial midbrain channel; PHBC = primordial hindbrain channel; SECs = scavenging endothelial cells. Liposomes formulated by extrusion (5 mM, 0.2% mol DOPE-LR). Scale bars: 200 µm (lateral view) and 100 µm (zoom).

hindbrain channels (PHBC) and cerebral arteries (CtAs)), but not all (*e.g.*, dorsal longitudinal vein (DLV), primordial midbrain channel (PMBC)) blood vessels and capillaries within the embryo head (**Figure 1d** and **Figure 2a)**. The specific blood vessels and capillaries in which PAP3 liposomes accumulated have been previously characterized as the brain endothelial cells (bECs), constituting the blood-brain-barrier (BBB) of the developing embryo.[41–43]

To verify selective liposome accumulation with bECs, PAP3 liposomes were administered (*i.v.*) within embryonic zebrafish at different developmental stages (2, 3 and 4 dpf) (**Figure 2b-d**). This two-day timeframe spans the onset and maturation of the embryonic BBB, most prominently within the mid- and forebrain, following complete hindbrain vascular invasion by 48 hpf (characterized by CtA capillary loops connecting both PHBCs with the central basilar artery (BA)).[41] Accordingly, at 2 dpf, PAP3 liposomes mainly accumulated in functional bECs, within blood vessels and capillaries of the hindbrain, namely CtAs, BA and PHBCs (**Figure 2b**). At 3 dpf, as blood vessels irrigate rostrally throughout the brain,[50] PAP3 liposomes accumulated within newly formed capillaries of the mid- and forebrain (**Figure 2c, e**), as well as within the continually expanding BBB vasculature of the hindbrain (**Figure 2f, h, i** and **Figure S1a-b** for a Z-stack depth color-coded of the vasculature in dorsal view). By 4 dpf, PAP3 liposomes extensively accumulated throughout the brain endothelium of the embryonic zebrafish (**Figure 2d**). Notably at all developmental stages, liposomes did not drastically accumulate in systemic blood vessels (*e.g.,* PMBC and DLV) within the head region (**Figure 2g**), confirming a specific preference of PAP3 liposomes for bECs at all developmental timepoints. Indeed, colocalization of PAP3 liposome accumulation and Claudin-5 expression, notably within the CtAs, MMCtA (**Figure 2h-i**) and MsA, was confirmed in Tg*(cldn5a:*eGFP*)*[42] embryos, stably expressing an integrated eGFP-Claudin5a fusion protein (**Figure 2j-k** and **Figure S1c**). In addition to bEC target selectivity, PAP3 liposomes also accumulated in the tail within the caudal hematopoietic tissue (CHT) and caudal vein (CV) of the embryo (**Figure 1a, b**). We have previously shown that these blood vessels are composed of scavenger endothelial cells (SECs) and blood resident macrophages, equivalent to hepatic reticuloendothelial (RES) cells (*i.e.,* liver sinusoidal endothelial cells (LSECs) and Kupffer cells (KCs)) in mammals.[38] SECs, in particular, proficiently recognize and clear anionic nanoparticles, as well as neutral DSPC liposomes, from circulation *via* the conserved scavenger receptors, Stabilin-1 and -2.

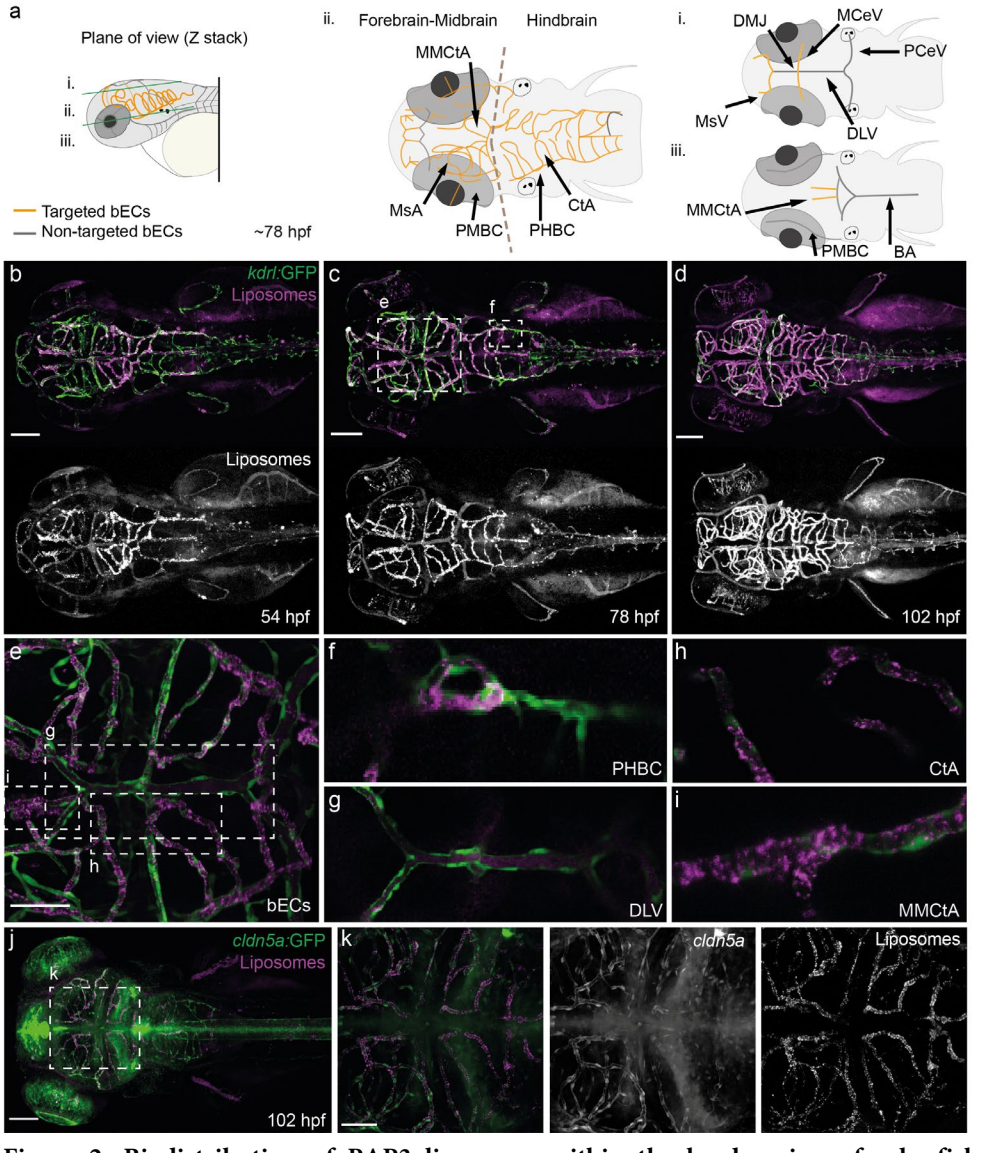

Figure 2. Biodistribution of PAP3 liposomes within the head region of zebrafish embryos. a) Schematic zebrafish larvae with key blood vessels in different planes of view. See **Figure S1a-b** for a Z-stacks depth color-coded zebrafish vasculature. Dorsal view, showing the **i.** top, **ii.** middle and **iii.** bottom layer diagram. The vasculature as follows, targeted brain endothelial cells (bECs) in yellow and non-targeted systemic endothelium in dark gray, at ~78 hpf. PHBC = primordial hindbrain channel; CtA = central artery; DLV = dorsal longitudinal vein; MsA = mesencephalic artery; MsV = mesencephalic vein; MMCtA = middle mesencephalic central artery. **b)** Biodistribution (10x magnification, dorsal view, 1.5 hpi) of PAP3 liposomes within the head region of a Tg(*kdrl:*GFP) zebrafish embryo at 54

hpf, **c)** 78 hpf, **d)** 102 hpf. **e)** High magnification view of **c** (inset, 40x, zoom) showing PAP3 liposomes accumulating within bECs. **f)** Posterior part of the PHBC, **g)** DLV, **h)** CtA, **i)** MMCtA. **j-k)** Biodistribution of PAP3 liposomes in a Tg*(cldn5a:*GFP*)*[42] zebrafish embryo (102 hpf) with GFP-labeling in blood and choroid plexus brain barrier showing colocalization of *cldn5a* with fluorescent liposomes. Zoom in of the region that includes the hindbrain vasculature and colocalization with *cldn5a* expression is shown in **Figure S1c**. Liposomes formulated by extrusion (5 mM, 0.2 mol% DOPE-LR). Scale bars: 100 µm (dorsal view), 50 µm (tissue level).

Accordingly, systemic administration of DSPC-containing PAP3 liposomes in zebrafish mutants lacking functional scavenger receptors Stabilin-1 and Stabilin-2 (*stabilin-1*^{ibl3} *stabilin-2*^{ibl1})[39] resulted in reduced liposome accumulation within the CHT and CV of the embryo without significantly affecting bEC targeting (**Figure S2**). This confirmed that (off-)targeting of PAP3 liposomes to RES-like cell types, but not bECs, was, at least in part, Stabilin-dependent. However, persistent liposome accumulation within blood resident macrophages of the mutant *stabilin-1/-2* double knockout embryo, suggested potentially significant and competitive pathways of PAP3 RES clearance.

Cryo-TEM revealed a novel 'parachute' liposome morphology that is essential for BBB targeting in embryonic zebrafish

To rationalize bEC-liposome specificity, and in the absence of any additional targeting functionality (*e.g.,* targeting ligands), cryogenic transmission electron microscopy (cryo-TEM) was performed to characterize PAP3 liposome ultrastructure. Unexpectedly, these images revealed a highly unusual phase-separated, "parachute" morphology, characterized by a single electron-dense protrusion within each liposomal membrane (**Figure 3a-c** and **Figure S3**). Such parachute-like structures have been previously reported for lipid-polymer hybrid nanoparticles,[51,52] propofol-containing liposomes,[53] and mRNA encapsulated LNPs[54,55] but, to the best of our knowledge, have not been reported for purely lipidic nanoparticles. Given the flat, bilayer preference of amphipathic DSPC, the observed phase-separated protrusion was hypothesized to be rich in DOaG. Indeed, at a molecular level, DOaG is structurally very similar to diacylglycerols (DAGs) whose hydrophobicity and geometry are known to alter the spontaneous curvature of PC

lipid membranes and perturb lamellar membrane structures resulting in the formation of non-bilayer phases.[56–60]

To investigate the possible association of phase separation and liposome-bEC selectivity, PAP3 liposomes were formulated at varying molar ratios (10-50 mol% DOaG) to correlate liposome morphology with *in vivo* biodistribution (**Figure 3d-i**). Of note, >50 mol% DOaG resulted in liposome aggregation. Cryo-TEM images of 10% DOaG liposomes (10-90 mol% DOaG-DSPC) revealed a mixture of non-spherical, bi-layered and multilamellar particles with no evident phase separation (**Figure 3d** and **Figure S4a**). 10% DOaG liposomes mostly accumulated within SECs in the CV and CHT of the embryo (**Figure S5a**) and did not target bECs (**Figure 3e**). Likewise, 20% DOaG liposomes (20-80 mol% DOaG-DSPC) were predominantly non-spherical (**Figure 3f** and **Figure S4b**), mainly accumulated within SECs (**Figure S5b**) and did not target bECs (**Figure 3g**). However, at 20% DOaG, small electron-dense protrusions within the liposome membrane indicated a liposome formulation approaching its miscibility threshold (**Figure 3f, Figure S4b** – white arrows). This was confirmed by the clear phase separation of 30% DOaG liposomes (30-70 mol% DOaG-DSPC) in which a single lipid protrusion was now clearly evident within each discreet liposome membrane (**Figure 3h, Figure S4c**). 30% DOaG liposomes, as for PAP3 liposomes (*i.e.,* 50-50 mol% DOaG-DSPC), proficiently targeted bECs of the zebrafish larvae (**Figure 3i** and **Figure S5c**). A 30 mol% DOaG miscibility threshold (within a DSPC bilayer) closely mirrors that previously reported for structurally similar DAGs (*i.e.,* 25 mol% miscibility threshold within a PC bilayer).[61]

Accordingly, to better understand the molecular details of DOaG lipid that facilitate the phase separation, we replaced the amide bond in DOaG to an ester bond, resulting in the naturally occurring diacylglycerol analogue, dioleyolglycerol (DOG). This also led to phase-separated liposomes and bEC targeting (**Figure S6a-d**). However, creating an analogue with two amides or replacing the oleic chains to stearyl chains (**Figure S6e-f**) resulted in lipids which cannot formulate liposomes. In addition, lipid phase separation is known to be dependent on the gel phase state

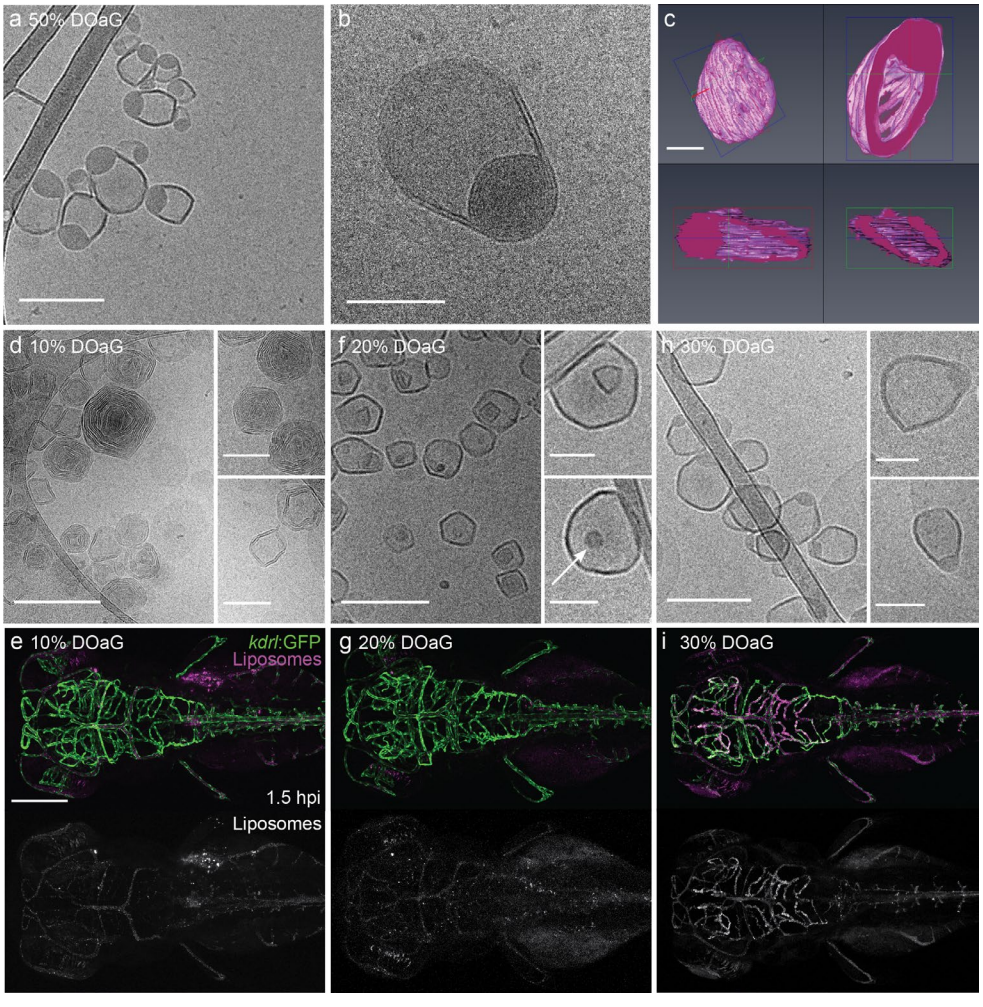

Figure 3. Cryo-TEM images of PAP3 liposomes and correlation of morphology with bECs targeting in zebrafish larvae (~78 hpf). a-b) Cryo-TEM images of PAP3 (50-50 mol% DOaG-DSPC) liposomes and **c)** 3D model of a representative PAP3 liposome, reconstructed based on the electron density derived from cryo-electron tomography, demonstrating the whole body and different plane sections of the particle**.** Cryo-TEM and biodistribution (in a Tg*(kdrl:*GFP*)* zebrafish embryo at 1.5 hpi) of liposomes containing DSPC and **d-e**) DOaG 10 mol%, **f-g)** 20 mol%, and **h-i)** 30 mol%. Liposomes (5 mM, 0.2% mol DOPE-LR) described in all panels formulated by ethanol injection except panel **b** and **c** - formulated by extrusion. Scale bars: 200 nm and 100 nm for higher magnification insets for cryo-TEM, 100 nm for 3D reconstruction and 200 μm for dorsal zebrafish view.

of a lipid bilayer. Consequently, switching co-formulant phospholipid from saturated DSPC (phase transition temperature (T*m*) 55°C) to unsaturated DOPC (T*m* -17°C) resulted in liposomes (at room temperature) with no apparent phase separation and severely ablated bEC targeting (**Figure S7**). Notably, incorporation of polyethylene glycol (PEG)-conjugated lipid (*e.g.* 1,2-distearoyl-sn-glycero-3-phosphatidylethanolamine DSPE-PEG, 5 mol% as commonly used)[62,63] to the PAP3 liposome results in the loss of selective targeting, as observed in the zebrafish (**Figure S8a-b**). Altogether, these experiments confirmed the critical requirement of phase-separated lipid protrusions for bEC selective liposome accumulation within the embryonic zebrafish.

PAP3 liposome targeting and uptake by bECs in zebrafish larvae is mediated by (endothelial) lipase

In the absence of any additional targeting functionality (*i.e.,* targeting ligands), we next investigated whether PAP3 liposomes could be hijacking an endogenous plasma lipid transport pathway to selectively target bECs of the embryonic zebrafish. Importantly, all major elements of mammalian plasma lipid transport and metabolism, including the expression of apolipoproteins, lipoprotein receptors (*e.g.*, low density lipoprotein receptor, LDLr) and hydrolytic enzymes (*e.g.*, lipases), are present and functional in a three day old zebrafish embryo.[64–66] These conserved features have led to the zebrafish being used as an *in vivo* model to investigate various lipid disorders,[67–69] including hypertriglyceridemia, a disease caused by a malfunction in lipase-mediated plasma lipid transport and metabolism.[70] Following secretion into blood, the typical first step of lipoprotein-mediated plasma lipid transport is the binding of soluble apolipoproteins.[1] To identify serum proteins preferentially adsorbed to PAP3 liposomes, we performed a photoaffinity-based capture of the PAP3 liposome protein corona.[71] For consistency, this experiment should be performed using zebrafish serum collected during embryonic stages; however, given the practical difficulties in obtaining sufficient embryonic zebrafish serum, these experiments were performed in human serum and do not necessarily reflect the exact composition and abundance of serum proteins in the developing zebrafish embryo. Importantly, functional conservation between the most abundant serum proteins in humans and zebrafish has been previously reported, including

similar profiles in apolipoproteins and complement proteins.[72] For this method, it was necessary to incorporate the photoaffinity probe, IKS02 (5 mol%),[71] within the PAP3 liposome formulation. Incorporation of this probe did not significantly alter the physicochemical properties or *in vivo* behavior of PAP3 liposomes (**Table S1**). Following protein corona capture, isolation and subsequent proteomic analysis, we identified soluble apolipoproteins as the major protein corona components of both PAP3 and control (100% mol) DSPC liposomes (**Figure S9**). However, while no obvious differences in protein corona composition could easily explain the very different *in vivo* fates of these two liposome formulations, a significant enrichment of apoA1, A4 and apoE on the surface of both PAP3 and DSPC liposomes, at least, conformed to a lipoprotein-like transport and metabolism targeting rationale.

Given the presence of apolipoproteins on the surface of PAP3 liposomes, we next investigated the potential role of extracellular, TG lipases in the selective accumulation of PAP3 liposomes at the BBB of the zebrafish larvae. Lipases are heparin-releasable[24,73] and following heparin pre-injection (*i.v.*; 30 minutes prior to PAP3 liposome administration), PAP3 liposomes remained freely circulating with no apparent bEC targeting (**Figure 4a-f**). While this suggested TG lipase involvement, heparin is also known to bind a wide range of other proteins that could (in)directly disrupt liposome-bEC accumulation.[74] We therefore selectively inhibited TG lipase enzymatic activity using the small molecule inhibitor, XEN445.[75,76] Following XEN445 pre-treatment (1 nL, 50 μM at 24 h and 1 h prior to PAP3 liposome administration), we observed a significant decrease in bEC targeting of liposomes. This result confirmed TG lipases play a fundamental role in determining the fate of PAP3 liposomes within the embryonic fish (**Figure 4g-i**).

Surprisingly, however, we found that PAP3 liposomes associated with bECs were no longer heparin-releasable (**Figure 5a-c**). This indicated that PAP3 liposomes, following initial lipase interaction, were internalized by bECs. To confirm this hypothesis, we incorporated the (endosomal) pH-sensitive dye, pHrodo™, within the PAP3 liposome membrane *via* a phospholipid anchor (as in reference [37]) (see **SI** for characterization and **Figure S10** for pH-dependent emission).

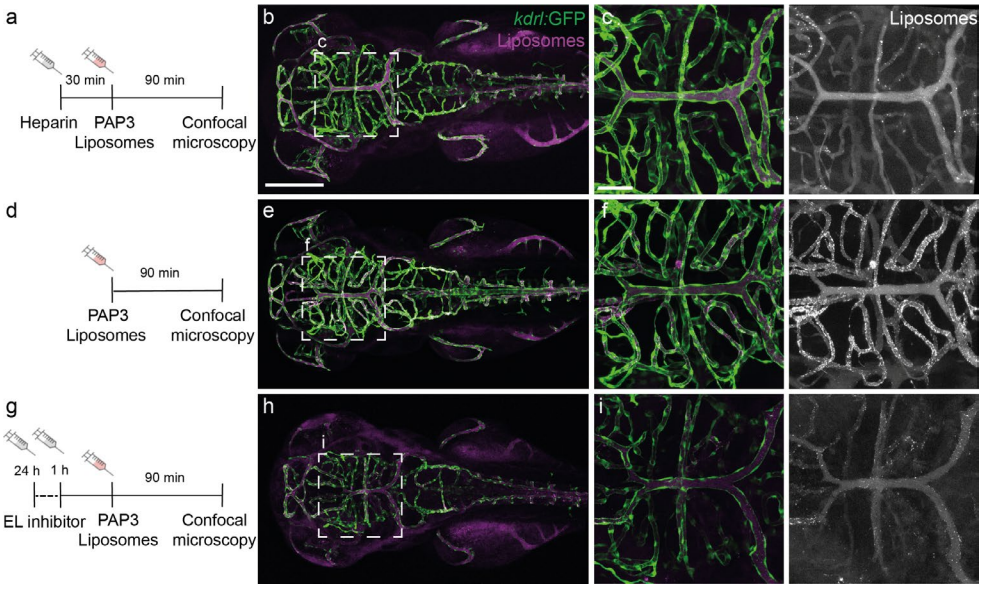

Figure 4. bECs targeting by PAP3 liposomes is inhibited by heparin and an TG lipase inhibitor. a) Timeline of injection and imaging. **b-c)** Biodistribution (10 and 40x magnification) of PAP3 liposomes at 1.5 hpi, after heparin (1 nl, 50 mg/ml) administration. **d)** Timeline of injection and imaging. **e-f)** Biodistribution (10 and 40x magnification) of PAP3 liposomes, as a reference, at 1.5 hpi. **g)** Timeline of injection and imaging. **h-i)** Biodistribution (10 and 40x magnification) of PAP3 liposomes at 1.5 hpi, after a double administration (24 h and 1 h prior liposome injection) of a TG lipase inhibitor (XEN445, 1 nL, 50 μM). All zebrafish larvae, Tg*(kdrl:*GFP*)* at ~78 hpi. Liposomes (5 mM, 0.2% mol DOPE-LR) formulated by extrusion. Scale bars: 200 μm (whole embryo) and 50 μm (tissue level).

Incorporation up to 0.5% mol of this fluorescent probe did not significantly alter the size or bEC targeting proficiency of PAP3 liposomes (**Table S1**). Following liposome administration, pHrodo™-associated fluorescence was clearly observed within bECs, *e.g.* CtAs and MMCtA, but not the systemic endothelium, *e.g.* DLV or PMBC (**Figure 5e-f**), mirroring the observed biodistribution of PAP3 liposomes and confirming PAP3 liposomes are endocytosed by bECs following initial lipase-liposome interaction.

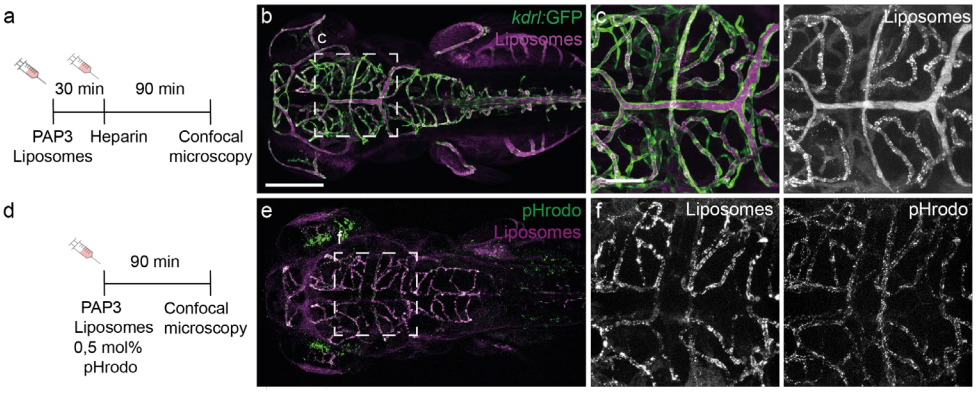

Figure 5. Internalization of PAP3 in zebrafish bECs. a) Timeline of injection and imaging. **b-c)** Biodistribution (10 and 40x magnification) of PAP3 liposomes (5 mM, 0.2 mol% DOPE-LR) after post-administration of heparin (1 nl, 50 mg/ml) in a Tg(kdrl:GFP) zebrafish embryo at 1.5 hpi. **d)** Timeline of injection and imaging. **e-f)** Biodistribution of PAP3 liposomes (10 mM), containing 0.5 mol% of pH sensitive DOPE-pHrodo (green/grey) to indicate endocytosis and 0.5 mol% of pH non-sensitive dye DOPE-NBD (magenta/grey) to label liposomes, in a AB/TL zebrafish embryo at 1.5 hpi. All zebrafish larvae at ~78 hpi. Liposomes formulated by extrusion. Scale bars: 200 µm (whole embryo) and 50 µm (tissue level).

PAP3 liposomes accumulate within the liver and spleen in mice, mediated (partially) by triglyceride lipase

Finally, we quantified the dynamic biodistribution of systemically administered PAP3 liposomes in 6-8 week old male mice. For these experiments, both XEN445 pre-treated (30 mg/kg XEN445 orally *b.i.d.* for 9 days prior to liposome administration) and untreated mice were used. As positron emission tomography (PET) tracer, a non-exchangeable ^{64}Cu ($T_{1/2}$= 12,7 h) radionuclide was incorporated within the PAP3 liposome formulation, chelated *via* the lipid-NOTA conjugate, NOTA-Bz-SCN-C18 (0.2 % mol). Based on 'cold' experiments using stable Cu isotopes, the incorporation of this lipid and/or Cu chelation protocol did not affect the physicochemical properties, morphology and/or bEC targeting proficiency of PAP3 liposomes in embryonic zebrafish (**Figure S11**, **Table S1**). Of note, phase-separation on PAP3 liposomes is also maintained upon incubation in mouse serum (**Figure S12**). Following tail vein injection (2845 ± 185 and 2480 ± 260 kBq/100 µL,

XEN445 treated and non-treated mice respectively; n=2 per group), PET scans were obtained, from 1 min to 6 hours post-injection, to visualize liposome biodistribution (**Figure 6a**). These values were corroborated through *ex vivo* radioanalysis (% ID/g, n=3) of the (major) organs (heart, brain, liver, spleen, kidneys, lungs, stomach and testes) and blood, following cardiac perfusion and organ collection at 10 min, 2 h and 6 hpi (**Figures 6b, c** and **Figure S13**). This data revealed rapid and extensive liposome accumulation within the murine liver (*ca.* 53% ID/g, 10 min post-injection) and spleen (*ca.* 106% ID/g) with low levels of PAP3 liposome accumulation in all other organs.

Following XEN445 pre-treatment (n=3 per time point), however, a significant increase of liposomes in circulation was observed at 2 h and a significant decrease in liposome accumulation within the murine liver, but not the spleen, was observed (**Figure 6b, c**). This reduction in PAP3 liposome liver accumulation, following small molecule TG lipase inhibition, confirmed at least a partial role for (endothelial) lipase in determining the fate of systemically administered PAP3 liposomes in mice. However, the failure of XEN445 to reduce liposome uptake in the spleen, as well as negligible PAP3 liposome accumulation in other EL-expressing organs (*e.g.,* lungs and testes), was equally indicative of significant 'off-target' and lipase-independent pathways of PAP3 liposome processing within RES organs of the mouse. As observed in the zebrafish embryo (**Figure 1b**), these 'off-target' interactions in the murine liver and spleen are most likely mediated by scavenging cell types, namely LSECs, KCs and splenic macrophages,[77,78] and these interactions are, in turn, mediated by a distinct array of receptors and enzymes, including Stabilins, class B scavenger receptors, ATP-binding cassette transporters, as well as TG lipases. To this end, it is noteworthy that apoA1-decorated nanobiologics have been specifically developed to preferentially target myeloid cells, notably in the liver and spleen.[79–81]

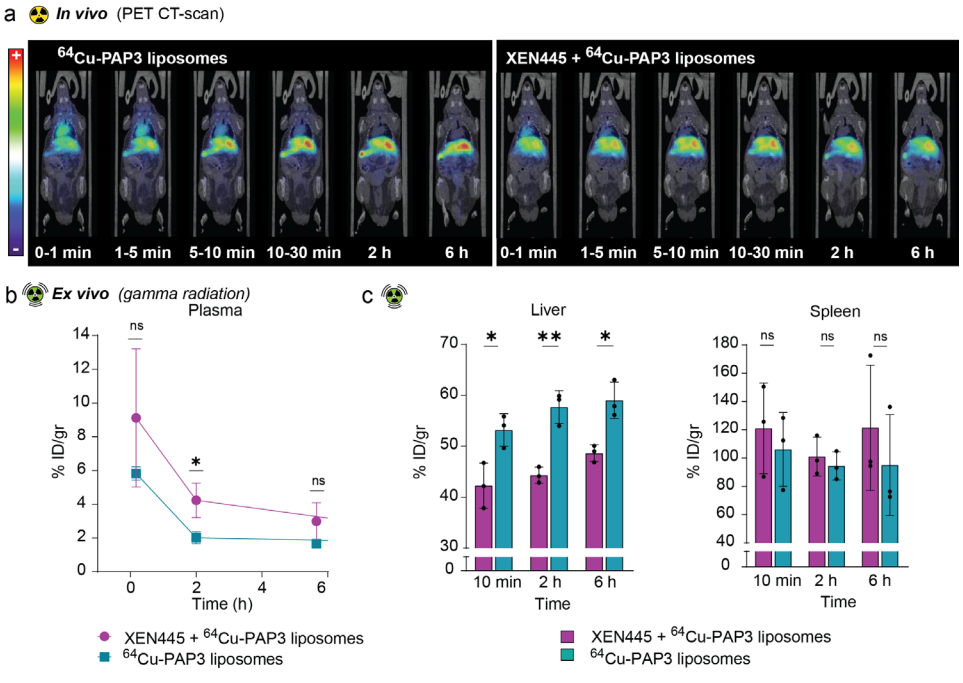

Figure 6. Biodistribution of radiolabeled PAP3 liposomes in mice. a) Representative positron emission tomography (PET) images (coronal projections) obtained at 0-1, 1-5, 5-10, 10-30 min, 2 h and 6 h after injection of radiolabeled PAP3 liposomes containing 0.2 mol% of ^{64}Cu-NOTA-Bz-SCN-C18 in 6-8 weeks male mice treated (or not treated) with XEN445 (30 mg/kg orally, *b.i.d.* for 9 days) prior to liposomal injection (n=2 per group and timepoint). PET images have been co-registered with representative CT slices for anatomical localization of the radioactive signal. **b)** *Ex vivo* gamma radiation counter of plasma in mice treated (or not treated) with XEN445. Concentration of radioactivity in plasma at 10 min, 2 h and 6 h after *i.v.* administration of radiolabeled PAP3 liposomes (n=3 per time point). **c)** *Ex vivo* gamma radiation counter of liver and spleen in mice treated (or not treated) with XEN445 at 10 min, 2 h and 6 h after *i.v.* administration of radiolabeled PAP3 liposomes (n=3 per group and time point). Statistical significance was evaluated using a two-tailed unpaired Student's t-test. ns: not significant ($P > 0.05$). Significantly different *$P < 0.05$, **$P < 0.01$; ***$P < 0.001$. Exact P values for **b**: 0.2379, 0.0242, 0.1095. Exact P values for **c**: 0.0259, 0.0029, and 0.0103 at 10 min, 2 h and 6 h respectively for the liver and 0.5668, 0.5323, 0.4659 for the spleen.

2.3 Discussion and Conclusion

Herein, we describe a liposome formulation, consisting of just two lipids, that is capable of hijacking an endogenous lipase-mediated pathway of lipid transport and metabolism to selectively target, and be taken up by, specific subsets of endothelial cells. While lipases, in particular small secretory phospholipase A_2 (sPLA2), have been previously exploited to achieve localized, stimuli-responsive drug release within target tissues (*e.g.*, solid tumors),[82,83] lipid nanoparticle targeting of TG lipases has, to the best of our knowledge, not been described before.

Lacking any additional targeting functionality, lipase recognition of PAP3 liposomes is mediated through a unique phase-separated, 'parachute' morphology. Such extreme phase-separated morphologies have not been described before for purely lipid nanoparticles. The discrete lipid-rich protrusion of each liposome resembles, in both structure and size, a solid lipid nanoparticle (*i.e.,* lipoprotein-like) and, as for analogous DAG/PC lipid mixtures, is likely characterized by increased stress on the bended membrane and increased surface hydrophobicity.[84,85] Although stable in water and Tris Buffer (**Figure S14** and **Table S1**), PAP3 liposomes tend to aggregate in physiologically relevant saline-containing buffers (**Table S1**). This is in line with observations showing that increased DAG concentrations in PC bilayers decreases the ability of PC to coordinate sodium ions.[86] However, PAP3 liposomes are stable in serum (**Figure S12**). Presumably, this is due to the rapid adsorption of soluble apolipoproteins (apoA1, A4 and E) to the liposome surface, as is required for the stabilization of endogenous secreted lipoproteins.[1] While greater molecular understanding is required as to how these lipid-rich, phase-separated protrusions are stably incorporated within the PAP3 liposome membrane, their compositional simplicity, unique morphology and unprecedented *in vivo* behavior provides an important proof-of-concept of a selective, lipase-mediated uptake pathway *in vivo*.

A key outstanding question is the precise mechanism of PAP3 liposome recognition and uptake within endothelial cells following lipase interaction. Here, we propose three plausible pathways. Pathway 1 – TG lipase binds to and directly internalizes PAP3 liposomes *via* cell surface proteoglycans (*e.g.* HSPG). This non-enzymatic, lipase-mediated pathway of endogenous lipoprotein uptake is known to be

particularly proficient in the case of lipase-mediated uptake of HDL particles.[22,34] Pathway 2 – TG lipase binds to PAP3 liposomes and acts as bridging molecule to a secondary receptor on the same cell, *e.g.,* apoER2, LRP1. Lipase-mediated bridging interactions are also known to facilitate lipoprotein intracellular uptake. [22,34,87] Pathway 3 – TG lipase binds to and enzymatically remodels PAP3 liposomes. Released PAP3 liposome metabolites are then recognized and internalized by alternative receptors expressed on target cells.

In zebrafish embryo, liposome selectivity for TG lipases is represented by bEC specific targeting, particularly for EL and LPL over HL. Expression of EL and LPL within the head of the zebrafish embryo is high from 2 to 4 dpf.[88,89] Together with the observed prevalence of ApoA1 -a cofactor of EL – on the PAP3 liposome surface (**Figure S9**) and XEN445 being 50-100 fold more selective inhibitor of EL (IC_{50} = 237 nM) over LPL (IC_{50} = 20 μM) and HL (IC_{50} = 9.5 μM).[75] This strongly suggests PAP3 liposomes preferentially hijack an EL-mediated pathway of endogenous lipoprotein recognition and metabolism.[21,31] We cannot however exclude the recognition of PAP3 liposomes similarly by other lipases, namely lipoprotein lipase (LPL) and hepatic lipase (HL) and by cell types other than endothelial cells due to competing interactions. In mice, EL expression is dynamically restricted in both time and space and is particularly high between embryonic stages E8.5 and E11.5 (but not later[90]) within the developing murine brain. In healthy adults, EL expression is mainly restricted to the lungs, liver, spleen, testes and ovaries (during pregnancy) and is particularly high in the placenta of pregnant mice.[21,31,90,91] A similar restricted pattern of EL expression has been reported in humans.[21]

Here, it is important to mention the significant decrease of PAP3 liposome uptake in the mouse liver after XEN445 treatment. This signifies the uptake acts – at least partially – as a liposome clearance mechanism via a lipase-mediated pathway. While other pathways, involving lipoprotein and more general scavenger receptors in hepatocytes and liver sinusoidal endothelial cells, as well as macrophage uptake via opsonization processes, are well established as lipid nanoparticle clearance mechanisms,[77] the role of TG lipases on nanoparticle clearance pathways, to our knowledge, has not been described before. However, additionally to the selective lipase-mediated clearance/uptake pathways, the significant competing off-target

interactions by liver and spleen have to be addressed and minimized to fully exploit this system. To this end, it will be fascinating to see if EL-mediated liposome targeting can be enhanced *via* local PAP3 liposome administration and/or dietary control of lipase expression.

Finally, this work again highlights the unique opportunities the zebrafish embryo can offer within nanomedicine discovery and development pipelines. Beyond the benefits of size, transparency, fecundity and ease of genetic manipulation,[92] in this case, the very discovery of ('irrational') PAP3 liposomes and the biological mechanism revealing the involvement of lipase-mediated pathways was only possible through our ability to screen and visualize large numbers of liposome formulations *in vivo*, at high resolution and across an entire living organism.

2.4 Materials and Methods

General reagents: 1,2-dioleoyl-*sn*-glycero-3-phosphocholine(DOPC), 1,2-distearoyl-*sn*-glycero-3 phosphocholine (DSPC), 1,2-dioleoyl-*sn*-glycero-3-phosphoethanolamine-N-(lissamine rhodamine B sulfonyl) (DOPE-LR) and NOTA-Bz-SCN-C18 (custom made), were purchased from Avanti Polar Lipids (Alabaster, AL, US). Additional DSPC was purchased from Lipoid GmbH. pHrodo™ Red, succinimidyl ester (pHrodo™ Red, SE) was purchased from Thermo Fisher Scientific. DOPE-pHrodo was synthesized as previously reported.[93] All other chemical reagents were purchased at the highest grade available from Sigma Aldrich and used without further purification. All solvents were purchased from Biosolve Ltd. Ultrapure MilliQ® water, purified by a MilliQ Advantage A10 water purification system from MilliPore, was used throughout. Heparin sodium salt from porcine intestinal mucosa, sodium carboxymethyl-cellulose (average Mw 90,000) and Tween 20 were purchased from Sigma Aldrich. XEN445 was purchased from AdooQ Bioscience (Irvine, CA, USA) and from Sigma Aldrich.

Synthesis and characterization of DOaG and DOG lipid: Column chromatography was performed using silica gel (40-63 μm, 60 Å, Screening Devices, The Netherlands). TLC analysis was performed on Merck silica gel 60/Kieselguhr

F254, 0.25 mm TLC plates. Compounds were visualized by KMnO4 stain (K_2CO_3 (15 g), $KMnO_4$ (2 g), and H_2O (200 mL)). 1 H spectra were recorded on a Bruker AV 400 MHz spectrometer. Chemical shifts are reported in ppm (δ), relative to the deuterated solvent as internal standard. Data are reported as follows: chemical shifts (δ), multiplicity (s=singlet, d=doublet, dd=doublet of doublet, td=triple of doublet, t=triplet, q=quartet, m=multiplet), coupling constants (J) reported in Hz. High resolution mass spectra were recorded by direct injection (2 μL of a 1 mM solution in methanol) using a mass spectrometer (Thermo Finnigan LTQ Orbitrap) with an electrospray ion source run in positive mode (source voltage 3.5 kV, sheath gas flow 10, capillary temperature 250°C).

2-hydroxy-3-oleamidopropyl oleate (Dioleoylamidoglycerol, DOaG)

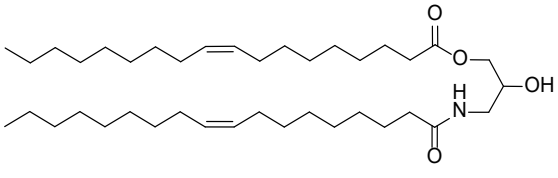

To a round bottom flask containing stirred solution of (±)-3-Amino-1,2-propanediol (100 mg, 1.10 mmol) in CH_2Cl_2:THF (5:1) (~15 mL), Oleic Acid (621.5 mg, 2.20 mmol), EDCI (527.1mg, 2.75 mmol), DMAP (336 mg, 2.75 mmol) and DIPEA (479 μL, 2.75 mmol) were added. After overnight stirring at room temperature (rt), the reaction mixture was diluted with DCM, washed with sat. NH_4Cl (~20 mL) and brine (~20 mL) and subsequently was dried (Na_2SO_4), filtered *in vacuo* and concentrated, so the crude compound was obtained. Purification by column chromatography (CH_2Cl_2 to 10% EtOAc in CH_2Cl_2) yielded the target material (248.5 mg, 0.40 mmol) isolated as a mixture of two regioisomers (substitution at 1° alcohol *vs.* 2° alcohol) at a ratio of 8:2 with a white waxy structure.

TLC (CH_2Cl_2: EtOAc, 8:2 v/v) : R_f = 0.3 ; **^{1}H NMR** (400 MHz, $CDCl_3$) δ 5.94 (t, *J* = 5.6 Hz, 1H), 5.40 – 5.28 (m, 4H), 4.86 – 4.78 (m, 0.2H), 4.15 (dd, *J* = 11.5, 5.2 Hz, 1H), 4.05 (dd, *J* = 11.5, 5.8 Hz, 1H), 3.97 – 3.88 (m, 0.8H), 3.64 – 3.46 (m, 1H), 3.27 – 3.19 (m, 1H), 2.34 (t, *J* = 7.6 Hz, 2H), 2.26 – 2.17 (t, *J* = 7.6 Hz, 2H), 2.00 (q, *J* = 6.4 Hz, 8H), 1.63 (dd, *J* = 11.1, 6.8 Hz, 4H), 1.28 (d, *J* = 14.6 Hz, 40H), 0.88 (t, *J* = 6.9 Hz, 6H) ; **ESI-HRMS** (m/z) $[M+H]^+$: calcd. for $C_{39}H_{73}NO_4$, 620.56; found 620.56, delta=0.1ppm.

2-hydroxypropane-diyl dioleate (Dioleoyl Glycerol, DOG)

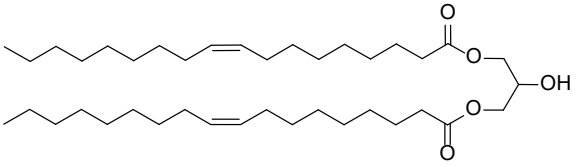

To a round bottom flask containing stirred solution of 1,2,3-Propanetriol (glycerol) (100 mg, 1.09 mmol) in CH_2Cl_2 : THF (5:1) (~15 mL), Oleic Acid (585 mg, 2.07 mmol), EDCI (527 mg, 2.75 mmol), DMAP (336 mg, 2.75 mmol) and DIPEA (479 µL, 2.75 mmol) were added. After overnight stirring at RT, the reaction mixture was diluted with DCM, washed with sat. NH_4Cl (~20 mL) and brine (~20 mL) and subsequently was dried (Na_2SO_4), filtered *in vacuo* and concentrated, so the crude lipid was obtained. Purification by column chromatography (CH_2Cl_2 to 2% EtOAC in CH_2Cl_2) yielded the target material (75.2 mg, 0.12 mmol) isolated as a mixture of two regioisomers (substitution at 1º alcohol *vs.* 2º alcohol) at a ratio of 8:2, as colorless oil.

TLC (CH_2Cl_2: EtOAc, 9.5:0.5 v/v) R_f = 0.8 ; **^{1}H NMR** (400 MHz, $CDCl_3$) δ 5.39 – 5.26 (m, 4H), 4.23 – 4.01 (m, 4.8H), 2.76 (t, *J* = 6.4 Hz, 0.2H), 2.34 (t, *J* = 7.6 Hz, 4H), 2.03 – 1.96 (m, 8H), 1.61 (dd, *J* = 14.6, 7.2 Hz, 4H), 1.28 (d, *J* = 14.3 Hz, 40H), 0.87 (t, *J* = 6.7 Hz, 6H).

Liposome formulation: Liposomes were formulated by extrusion or by ethanol injection (Note: DOPC:DOaG liposomes could be only formulated by ethanol injection) in ddH_2O at a total lipid concentration of 5 mM and containing 0.2 mol% DOPE-Lissamine Rhodamine (DOPE-LR) for fluorescent visualization, unless otherwise stated. In the case of extrusion, individual lipids as stock solutions (1-10 mM) in chloroform, were combined to the desired molar ratios and dried to a thin film, first under N_2 stream, then >1 h under vacuum. Lipid films were hydrated above the T_m of all lipids (65-70ºC), with gentle vortexing if necessary, to form a suspension. Large unilamellar vesicles were formed through extrusion (mini extruder, Avanti Polar Lipids) above the T_m of all lipids (*i.e.* 65-70ºC). Hydrated lipids were passed 11 times through 2 x 400 nm polycarbonate (PC) membranes (Nucleopore Track-Etch membranes, Whatman), followed by 11 times through 2 x 100 nm PC membranes. All liposomes were stored at 4 ºC and used within 1 week.

In the case of ethanol injection, lipid films were re-dissolved in absolute ethanol to a total lipid concentration of 50 mM. Using a glass micro-syringe (Hamilton, syringe series 700, volume 50 or 500 µl) 50 or 100 µL of the ethanolic solution was submerged in a water bath of 70 °C for 1-2 sec and then was rapidly injected in a glass vial containing 0.5 mL or 1mL ddH_2O, respectively, (1:10 v/v; EtOH:H_2O) at 70°C under constant vigorous stirring (650 rpm – stirring bar dimensions: 12 x 4 x 4 cm), to form large unilamellar vesicles. Liposomes were then transferred to a dialysis tube (Spectrum labs, 3.5k MWCO) or a dialysis cassette (slide-A-Lyzer™ 3.5k MWCO, Thermo Fisher Scientific) and dialyzed against ddH_2O overnight at 4°C, to ensure complete ethanol removal. All liposomes were stored at 4 °C and used within 1 week.

Size and zeta potential measurements: Particle size and zeta potentials were measured using a Malvern Zetasizer Nano ZS. For DLS (operating wavelength = 633 nm), measurements were carried out at room temperature in water at a total lipid concentration of approx. 100 µM. Zeta potentials were measured at 500 µM total lipid concentration, using a dip-cell electrode (Malvern), at room temperature. For liposomes formulated in water, aq. NaCl was added to the liposome solution to a final concentration of 10 mM before zeta potential measurement. All reported DLS measurements and zeta potentials are the average of three measurements.

Cryogenic transmission electron microscopy and 3D tomography: Liposomes (3 µL, 5 mM total lipid concentration) were applied to a freshly glow-discharged carbon 200 mesh Cu grid (Lacey carbon film, Electron Microscopy Sciences, Aurion, The Netherlands). Grids were blotted for 3 sec at 99% humidity in a Vitrobot plunge-freezer (FEI VitrobotTM Mark III, Thermo Fisher Scientific). Cryo-EM images were collected on a Talos L120C or a KRIOS (NeCEN, Leiden University) operating at 120 kV or 300 kV, respectively. In the case of Talos, images were recorded manually at a nominal magnification of 17500x or 28000x yielding a pixel size at the specimen of 5.83 or 3.56 ångström (Å), respectively. In the case of KRIOS, images were recorded manually at a nominal magnification of 33000x yielding a pixel size at the specimen of 3.48 ångström (Å). Alternatively, imaging and cryo-ET was performed on a Titan operating at 300kV (TU Eindhoven). Images were recorded manually at a nominal magnification of 6500x or 24000x yielding a pixel size at the specimen of 13.87 or 3.86 ångström (Å),

respectively. Tomographic tilt series acquisition was performed with Inspect3D software from Thermo Fisher Scientific with a total electron dose of less than 100 e/nm2. Alignment and reconstruction of the series were performed using IMOD[94] and Avizo 9 (Thermo Fisher Scientific).

Zebrafish husbandry and injections: Zebrafish (*Danio rerio*, strain AB/TL) were maintained and handled according to the guidelines from the Zebrafish Model Organism Database (http://zfin.org) and in compliance with the directives of the local animal welfare committee of Leiden University. Fertilization was performed by natural spawning at the beginning of the light period, and eggs were raised at 28.5 °C in egg water (60 μg/ mL Instant Ocean Sea salts). The following previously established zebrafish lines were used: Tg*(cldn5a:*eGFP)[42], Tg*(kdrl:*eGFP)^{s843},[95] Tg*(mpeg1:*GFP)^{gl22},[96] Tg*(mpeg1:*mCherry)^{gl23},[96] and a previously generated zebrafish mutant (*stabilin-1*^{ibl3} *stabilin-2*^{ibl1}).[39] Liposomes were injected into 54-120 hours post fertilization zebrafish embryos using a modified microangiography protocol.[97] Embryos were anesthetized in 0.01% tricaine and embedded in 0.4% agarose containing tricaine before injection. To improve reproducibility of microangiography experiments, 1 nl volume was calibrated and injected into the sinus venosus/Duct of Cuvier or the primary head sinus. A small injection space was created by penetrating the skin with the injection needle and gently pulling the needle back, thereby creating a small pyramidal space in which the liposomes were injected. Successfully injected embryos were identified through the backward translocation of venous erythrocytes and the absence of damage to the yolk ball. More details about the protocol used or injections in the zebrafish embryo are provided in reference [97]. Heparin (1 nl of 50 mg/ml) was injected 30 min before/after liposome injection. XEN445 (first dissolved in DMSO to obtain a 10 mM stock solution and then diluted in water to a final concentration of 50 μM) was administered 24 h and 1 h prior liposome injection.

Confocal imaging acquisition and editing: Zebrafish embryos were randomly picked from a dish of 20-60 successfully injected embryos. Confocal z-stacks were captured on a Leica TCS SPE or SP8 confocal microscope, using a 10x air objective (HCX PL FLUOTAR), a 40x water-immersion objective (HCX APO L) or 63x water-immersion objective (HC PL APO CS). For whole-embryo views, 3/4 overlapping z-stacks were captured to cover the complete embryo in lateral view.

Laser intensity, gain and offset settings were identical between stacks and each experiment. Images were processed and quantified using the Fiji distribution of ImageJ.[98,99]

Studies in mice: Male mice weighting *ca.* 18-20 g (C57BL6, 6-8 weeks, Janvier; see below for number of animals) were used. Animals were treated with 30 mg/kg XEN445 (as a suspension in 0.2% Tween-20/1% carboymethyl-cellulose) orally *b.i.d.* for 9 days[75] prior to liposome administration.

For radiolabeling studies, PAP3 liposomes (10 mM total lipid concentration) were made by ethanol injection as described above, with only difference that 0.2 mol% of NOTA-Bz-SCN-C18 (custom made, Avanti Polar Lipids) was added to the lipid film. Additionally, the required total volume of liposomes was made in two batches of 500 µl to ensure avoidance of aggregation. After formation of particles and removal of ethanol, $^{64}CuCl_2$ in 0.1 M aq. ammonium acetate pH=5.5 was added to the liposome solution and the mixture was incubated at room temperature (20 mins) (1:4 v/v ammonium acetate/liposomes). Subsequently, the free $^{64}CuCl_2$ was removed by size exclusion chromatography (SEC) (NAP™-25 columns Sephadex™, GE Healthcare) equilibrated with 10 mM Tris buffer pH=7.4. Elution fractions of 500 µl containing the radiolabeled liposomes were collected from the SEC column and their radioactivity was checked using a dose calibrator (CPCRC-25R, Capintec Inc., NJ, USA). The fraction containing the higher concentration of radioactivity was measured in size by DLS and was used for subsequent *in vivo* imaging and *ex vivo* studies.

For PET imaging studies, anesthesia was induced by inhalation of 3% isoflurane in pure O_2 and maintained by 1.5-2% isofluorane in 100% O_2. With the animal under anesthesia, the labelled liposomes were injected *via* one of the lateral tail veins (2845 ± 185 kBq/100 µl for treated animals; 2480 ± 260 kBq/100 µl for non-treated animals; n=2 per group). Dynamic whole-body images (20 min duration) were acquired list-mode in one bed position in a 511 keV ± 30% energetic window immediately after administration of the labelled liposomes using a MOLECUBES β-CUBE scanner. Static 10 min images were also acquired at 2 h and 6 h after administration. After each PET scan, whole body high resolution computed tomography (CT) acquisitions were performed on the MOLECUBES X-CUBE scanner, to provide anatomical information as well as the attenuation map for the later reconstruction

of the PET images. Dynamic PET images were reconstructed with OSEM-3D iterative algorithm, using the following frames: 4 × 30 s, 4 × 60 s, 4 × 120 s, 2 × 180 s. Static images were reconstructed as a single frame using the same method. Images were analyzed using π-MOD image analysis software (π-MOD Technologies Ltd, Zurich, Switzerland).

For *ex vivo* biodistribution studies, animals (n=3 per compound and time point) were anesthetized with isoflurane 3% isoflurane in pure O_2 and maintained by 1.5-2% isoflurane in 100% O_2. A solution containing the labelled liposomes (2640 ± 370 kBq/100 µl for treated animals; 2530 ± 385 kBq/100 µl for non-treated animals; n=3 per group and time point) was injected through one of the lateral tail veins. Animals were recovered from anesthesia and at pre-determined time points (t=10 min, and 2, 6 and 24 h), animals were anesthetized again and sacrificed by perfusion using saline solution and brain, liver, kidneys, spleen, lungs, heart, and stomach were quickly removed and rinsed with water. The amount of radioactivity in each organ was measured in an automatic gamma counter (2470 Wizard, PerkinElmer). Blood samples were obtained just before perfusion. Part of the blood was processed to separate the plasma, which was also counted in the gamma counter. Results were normalized to injected dose and organ weight to express the results as percentage of injected dose per gram of tissue (% ID/g).

Statistical analysis: All experiments performed in zebrafish embryo/larvae presented in this chapter were repeated at least twice and were performed using freshly prepared liposomes. For all experiments performed in zebrafish, at least four embryos were randomly selected (from a pooled of ~20-60 successfully injected embryos) and visualized at low resolution microscopy. From these four embryo/larva zebrafish, at least one was selected for confocal microscopy. The imaged zebrafish was representative for the data and showed consistent results confirming the presented data. No statistical analysis is performed in this work. All experiments performed in mice were approved by the ethical committee of CIC biomaGUNE and by local authorities (Diputación Foral de Guipúzcoa), authorization number PRO-AE-SS-207, maintained and handled in accordance with the guidelines and regulations (Guidelines for Accommodation and Care of Animals). Statistical analysis as follows: for the *ex vivo* gamma radiation studies, results were normalized to injected dose and organ weight to express the results as

percentage of injected dose per gram of tissue (% ID/g). Data is presented as mean ± SD values. Sample size used for mice studies was n=2 per group per timepoint for the PET images and n=3 per group per time point for the *ex vivo* gamma radiation experiments. Statistical significance was evaluated using a two-tailed unpaired Student's t-test. ns: not significant ($P > 0.05$). Significantly different *$P < 0.05$, **$P < 0.01$; ***$P < 0.001$. Exact P values are included in the figure captions. GraphPad was used as a software for the statistical analysis.

Protein corona analysis: Proteomic corona analysis of PAP3 and DSPC liposomes was performed as described in reference [71]. Briefly, liposomes were formulated by extrusion incorporating 5 mol% of the IKS02 diazirene-based photoaffinity lipid probe and incubated in human serum at 37°C for 1h (1:1 volumetric ratio). Proteins adsorbed to the surface of the liposomes were *in situ* photo-cross linked with the IKS02 probe of the liposomes. Afterwards, the captured proteins were isolated and quantified with LC-MS/MS.

2.5 Supplementary Information

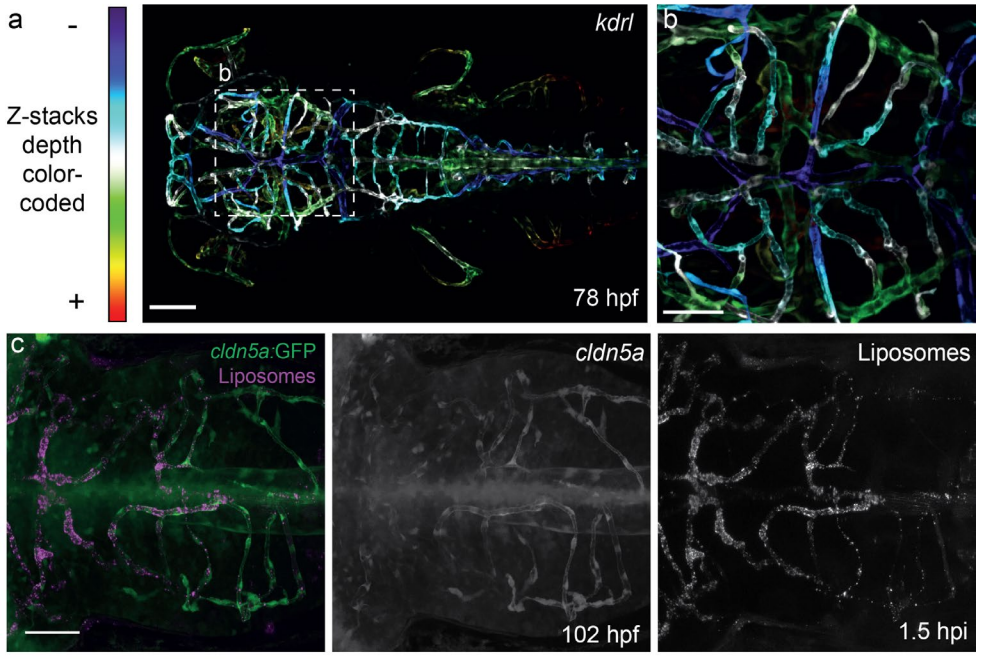

Figure S1. Vascularization within the head region of a zebrafish embryo (3 dpf) and biodistribution of PAP3 liposomes in Tg*(cldn5a:*eGFP) embryos (4 dpf). a-b) Depth color-coded z-stacks of the head region of a Tg(*kdrl*:GFP) zebrafish embryo, in dorsal view, at approx. 3 days post fertilization (dpf). Depth color scale: blue (dorsal) to red (ventral). **c)** Colocalization of *cldn5a* and PAP3 liposomes (5 mM, 0.2 mol% DOPE-LR) within the hindbrain region (magnification 40x, zoom) of a 4 day-old Tg*(cldn5a:eGFP)* zebrafish at 1.5 hpi (whole embryo, 10x shown in **Figure 2j**). Liposomes formulated by extrusion. Scale bars: 100 μm (a) and 50 μm (b-c).

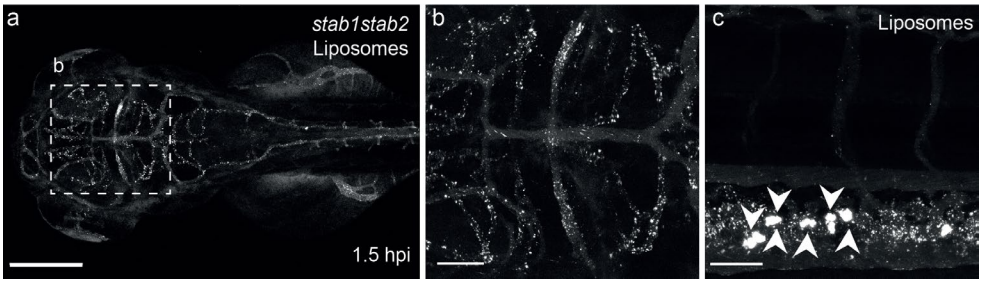

Figure S2. Biodistribution of PAP3 liposomes within *stabilin-1/-2* double knockout zebrafish embryos (3 dpf). a) Biodistribution (10x magnification) of PAP3 liposomes (5

mM, 0.2 mol% DOPE-LR) within the head region of a mutant *stab1*^{ibl3}*stab2*^{ibl1} zebrafish embryo at 1.5 hpi. **b)** High magnification (40x, zoom) dorsal view of PAP3 liposome biodistribution showing accumulation within bECs. **c)** High magnification (40x), lateral view, showing accumulation of PAP3 liposomes within blood-resident macrophages (white arrows) of the CHT of a mutant *stab1*^{ibl3}*stab2*^{ibl1} zebrafish embryo at 1.5 hpi. Liposomes formulated by extrusion. Scale bar: 200 µm (a) and 50 µm (b-c).

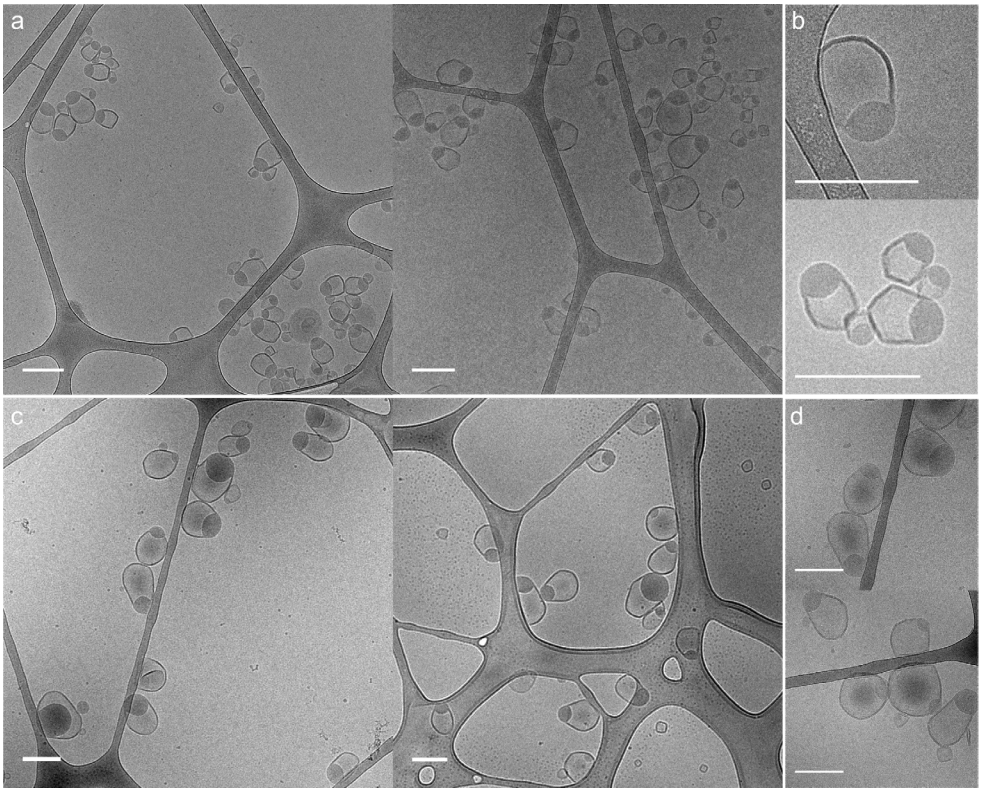

Figure S3. Cryo-TEM images of 'parachute' PAP3 liposomes formulated by two methods. a, b) PAP3 liposomes formulated by ethanol injection. **c, d)** PAP3 liposomes formulated by extrusion. Scale bars: 200 nm.

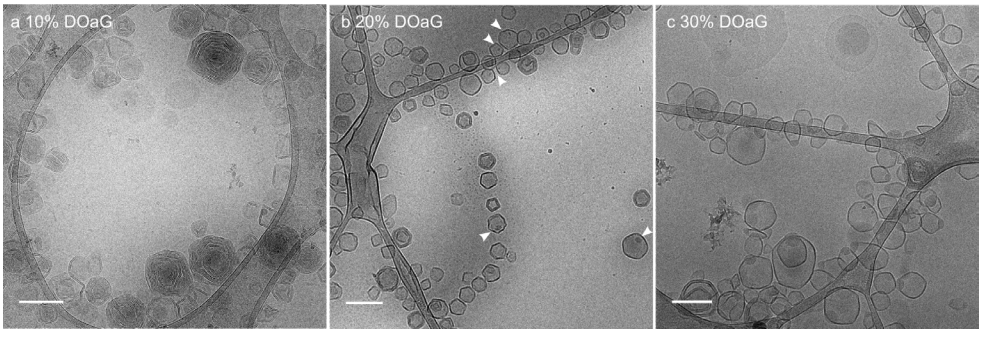

Figure S4. Cryo-TEM images of PAP3 liposomes formulated at varying molar ratios. Liposomes composed of DSPC and **a)** 10 mol%, **b)** 20 mol% or **c)** 30 mol% DOaG. White arrows indicate small electron rich protrusions. Liposomes formulated by ethanol injection. Scale bars: 200 nm.

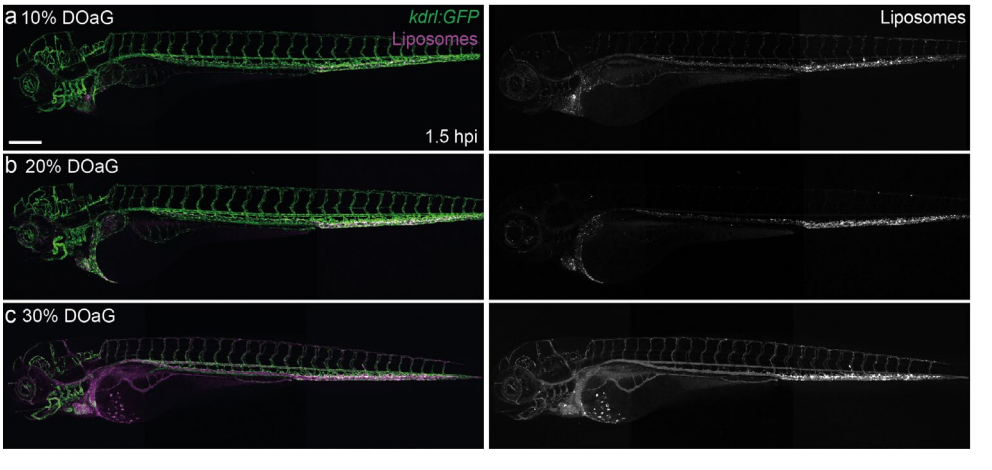

Figure S5. Biodistribution of PAP3 liposomes formulated at varying molar ratios within zebrafish embryos (3 dpf). a) Biodistribution (10x magnification) of liposomes (5 mM, 0.2 mol% DOPE-LR) composed of DSPC and 10 mol%, **b)** 20 mol%, or **c)** 30 mol% DOaG within the whole body of Tg(*kdrl*:GFP) zebrafish embryos at 1.5 hpi. Liposomes formulated by ethanol injection. Scale bar: 200 μm.

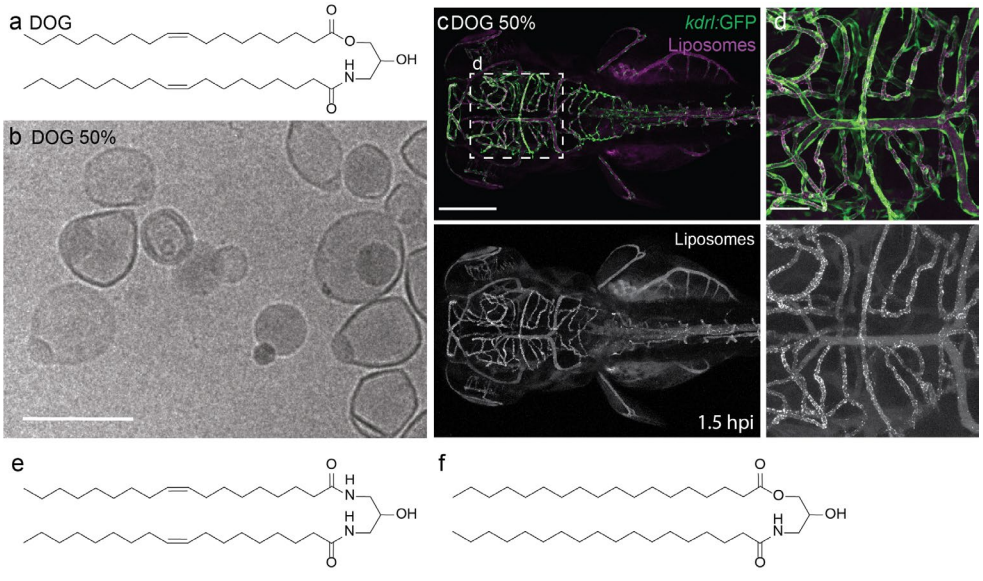

Figure S6. Cryo-TEM and biodistribution of DSPC:DOG liposomes within zebrafish embryos (3 dpf). a) Chemical structure of dioleoyl glycerol (DOG(18:1/0:0/18:1). **b)** Cryo-TEM of liposomes containing DSPC and DOG in equal ratios. **c)** Biodistribution (10x magnification) of DSPC:DOG liposomes (5 mM, 0.2 mol% DOPE-LR) within the head region of a Tg(*kdrl*:GFP zebrafish embryo at 1.5 hpi. **d)** High magnification (40x, zoom) view of DSPC:DOG liposome biodistribution showing accumulation within bECs. Liposomes formulated by extrusion. Scale bars: 200 nm (cryo-TEM), 200 µm (dorsal view) and 50 µm (tissue level). **e)** Chemical structure of variant with two amides. **f)** Chemical structure of variant with two stearyl chains.

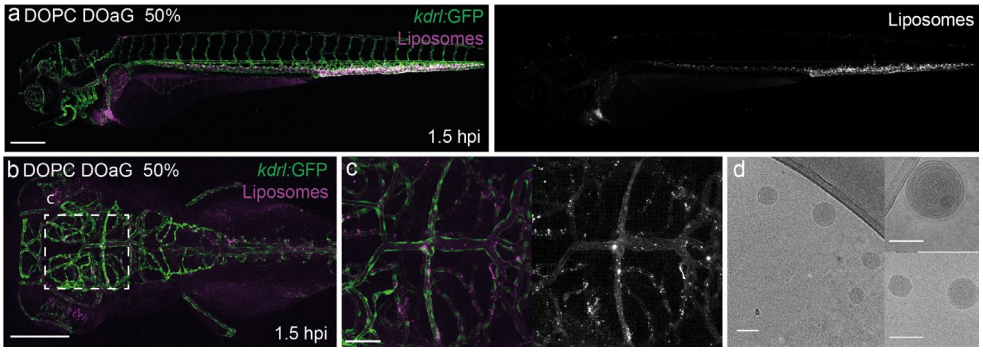

Figure S7. Cryo-TEM and biodistribution of DOPC:DOaG liposomes within zebrafish embryos (3 dpf). a) Biodistribution (10x magnification) of DOPC:DOaG liposomes (composed in equal ratios, 5 mM, 0.2 mol% DOPE-LR) within the whole body of a

Tg(*kdrl*:GFP) zebrafish embryo at 1.5 hpi. **b)** Dorsal view (10x magnification) of DOPC:DOaG liposome biodistribution within the head region. **c)** High magnification (40x, zoom) view of DOPC:DOaG liposome biodistribution showing no accumulation within bECs. **d)** Cryo-TEM images of DOPC:DOaG liposomes showing multilamellar with solid core or solid lipid-like morphology. Liposomes formulated by ethanol injection. Scale bars: 200 μm (dorsal and lateral views), 50 μm (tissue level) and 100 nm (cryo-TEM).

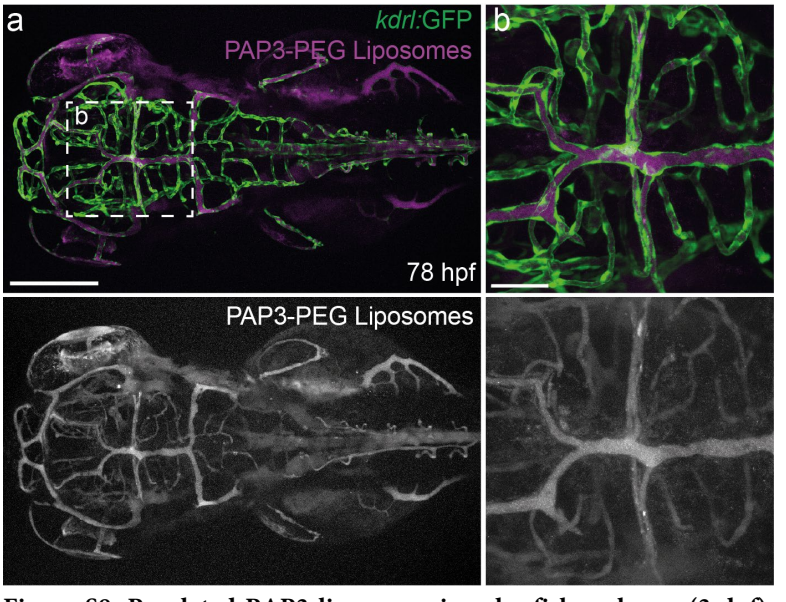

Figure S8. Pegylated-PAP3 liposomes in zebrafish embryos (3 dpf). a) Biodistribution (10x magnification) of PAP3 liposomes (5 mM, 0.2 mol% DOPE-LR) containing DSPE-PEG (5 mol%) in a Tg(*kdrl*:GFP) zebrafish embryo at 1.5 hpi. Liposomes formulated by extrusion. Scale bars: 200 μm (lateral view), 50 μm (tissue level).

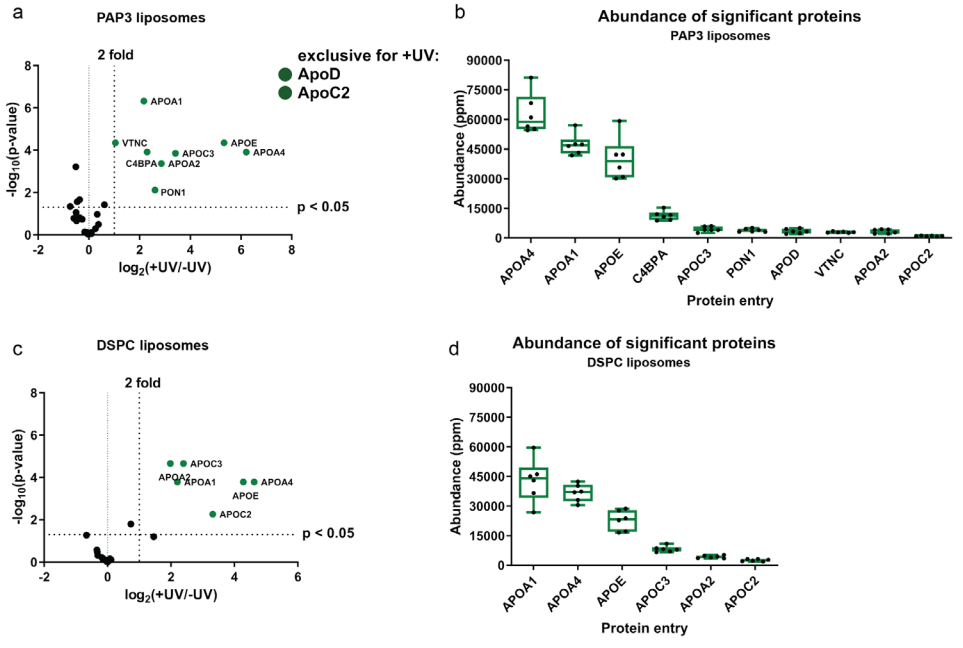

Figure S9. Identification of the PAP3 liposome protein corona, isolated via photoaffinity-based method. a, c) Volcano plots of enrichment over background (log_2(+UV/-UV) plotted against the statistical significance of this comparison (-log_{10}(*p*-value)) of PAP3 and 100% DSPC liposomes, respectively. Proteins meeting all selection criteria labeled in green. Proteins without background labeling are listed as exclusive for +UV. **b, d)** Abundance plots of proteins (replicate abundancies of the top10 proteins (ppm) withing the +UV samples) identified in PAP3 and DSPC liposomes respectively. Liposomes with affinity probe (IKS02 5 mol%) incorporated into the liposome membrane were formulated by extrusion.

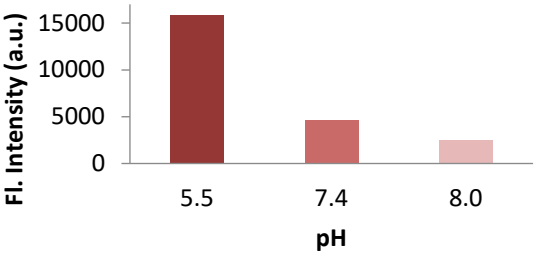

Figure S10. Fluorescence intensity of PAP3 liposomes containing 0.5% mol DOPE-pHrodo™ at different pH (5.5, 7.4 and 8.0). Fluorescence intensity of liposomes containing 0.5% mol DOPE-pHrodo™ in buffer solutions of different pH (ammonium acetate for pH 5.5, and Tris Buffer for pH 7.4 and 8.0) was measured on a plate reader at 585nm (ex/em of pHrodo™: 560/585nm).

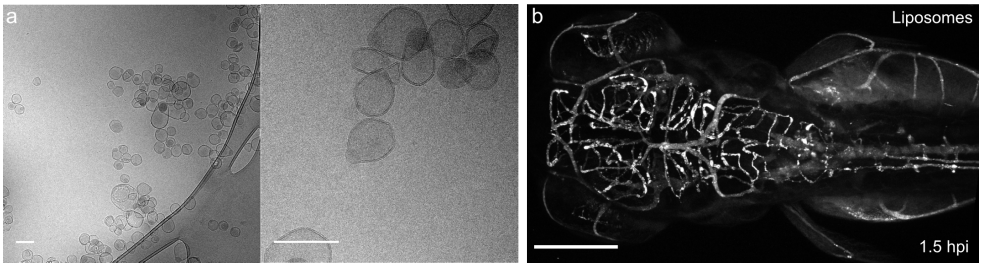

Figure S11. Cryo-TEM and biodistribution of ^{64}Cu - PAP3 liposomes containing NOTA-Bz-SCN-C18 within zebrafish embryos (3 dpf). a) Cryo-TEM images of PAP3 liposomes containing 0.2% mol NOTA-Bz-SCN-C18 after Cu chelation (stable Cu isotope). **b)** Biodistribution (10x magnification) of PAP3 liposomes (0.1% mol DOPE-LR, 0.2% mol NOTA-Bz-SCN-C18, after ^{64}Cu chelation) within the head region of an AB/TL zebrafish embryo at 1.5 hpi, showing accumulation in bECs. Two weeks after ^{64}Cu chelation and administration in mice (to ensure radioactivity decay), the remaining sample was injected in zebrafish embryos to confirm bEC targeting was retained. Liposomes containing NOTA-Bz-SCN-C18 were formulated by ethanol injection. Scale bars: 200 nm (cryo-TEM), 200 μm (dorsal view).

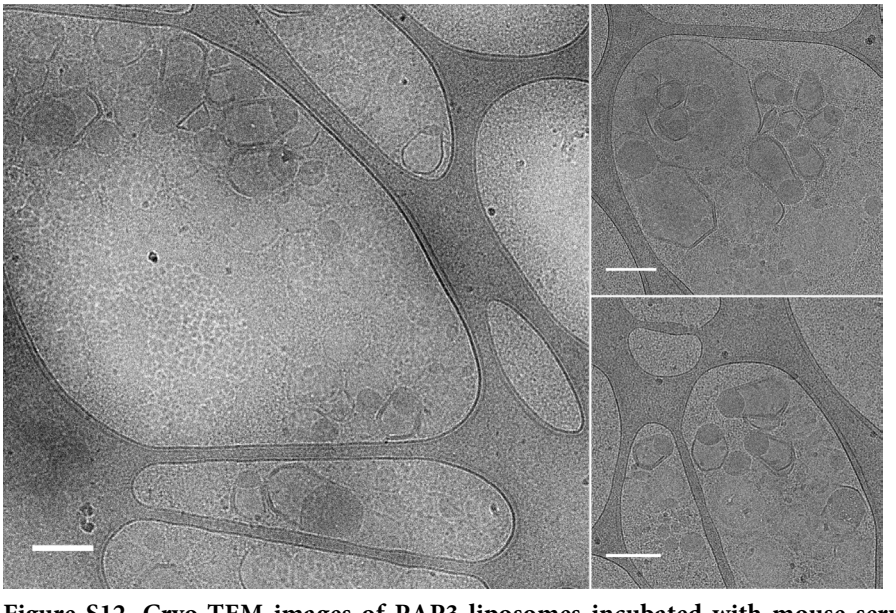

Figure S12. Cryo-TEM images of PAP3 liposomes incubated with mouse serum (2:1 volumetric ratio). Liposomes were incubated with mouse serum at 37 °C for 30 min. Liposomes formulated by extrusion. Scale bars: 200 nm.

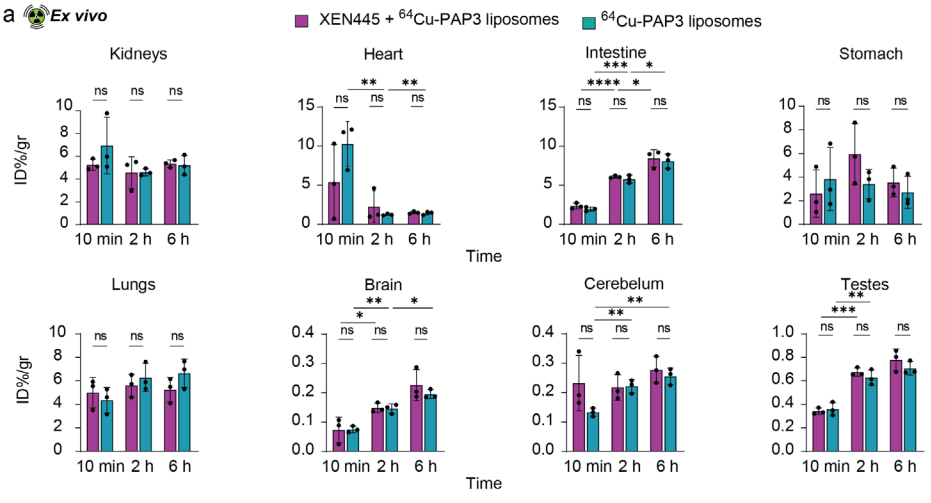

Figure S13. Biodistribution of radiolabeled PAP3 liposomes in male mice. a) *Ex vivo* gamma radiation counter (%ID/gr) of kidneys, heart, intestine, stomach, lungs, brain, cerebellum and testes in mice after XEN445 treatment or in mice without treatment at 10 min, 2 h and 6 h after *i.v.* administration of ^{64}Cu-labelled PAP3 liposomes (n=3 per group and time point). Statistical significance was evaluated using a two-tailed unpaired Student's t-test. ns: not significant (P > 0.05). Significantly different *P < 0.05, **P < 0.01; ***P < 0.001 and P<0.0001****. Exact P values for the heart 0.0057**, 0.0061**, for the intestine <0.0001****, 0.0003***, 0.0191* and 0,0237*; for the brain 0.0496*, 0.0033**, 0.0194*; for the cerebellum 0.0048** and 0.0024**; and for the testes 0.0002***, 0.0056**.

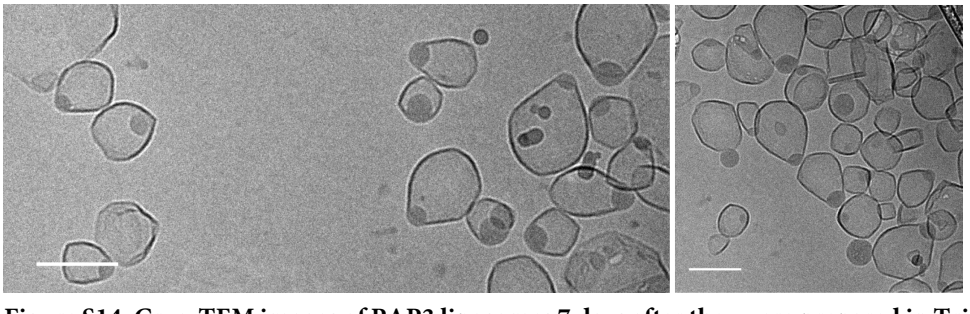

Figure S14. Cryo-TEM images of PAP3 liposomes 7 days after they were prepared in Tris Buffer. PAP liposomes were prepared by extrusion in 10mM Tris Buffer pH = 7.4 and cryo-TEM images were taken 7 days after preparation.

Chemical characterization – ^{1}H-NMRs

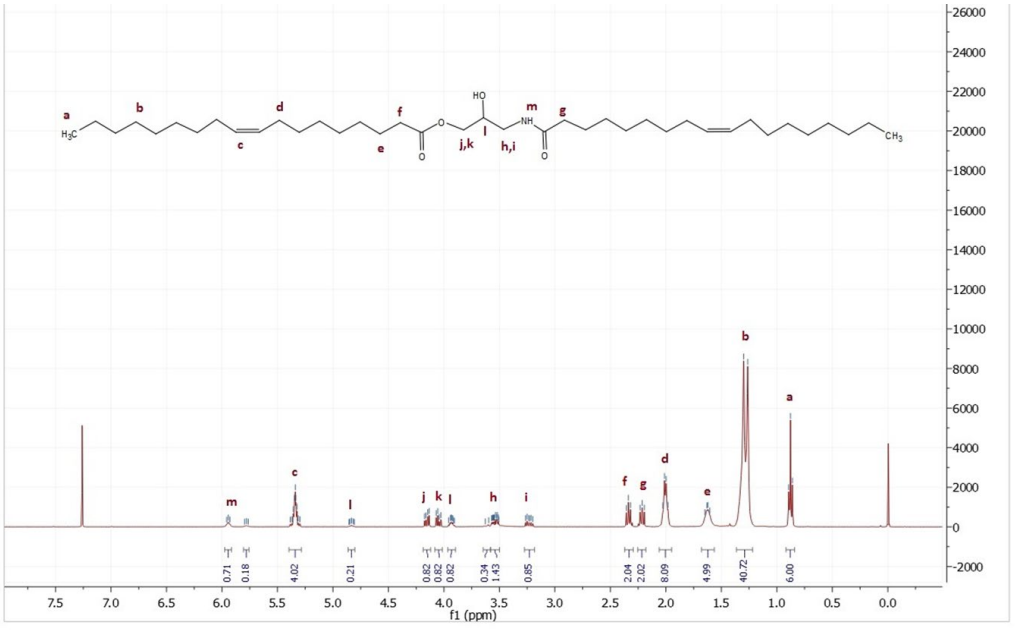

^{1}H-NMR of DOaG

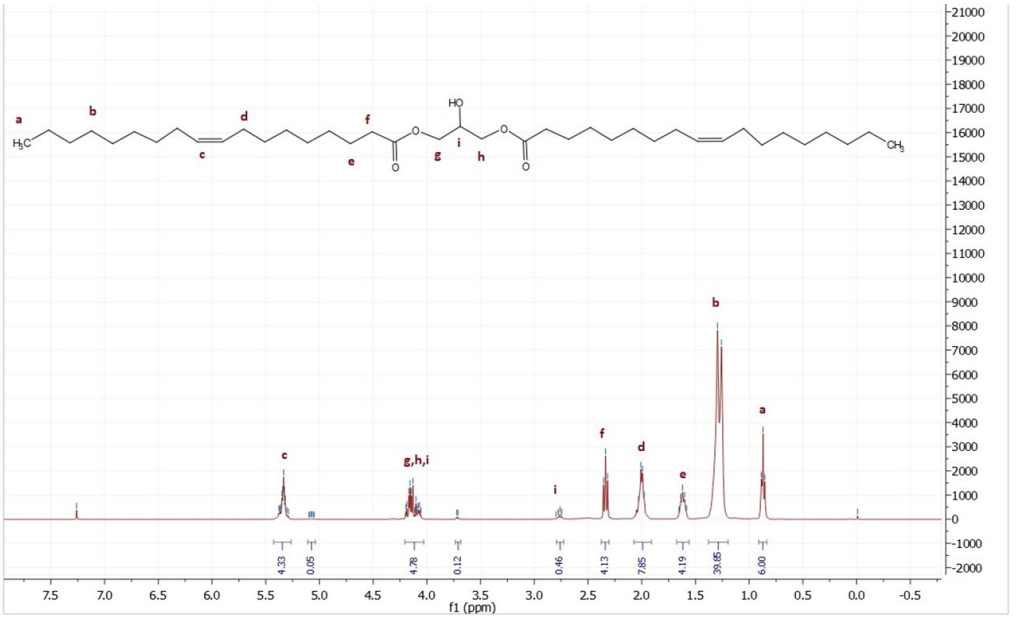

^{1}H-NMR of DOG

Table S1. Physicochemical properties of liposomes

Formulation	Preparation method		Size (nm)	PDI	ζ-potential* (mV)
10% DOaG liposomes	Ethanol injection		± 137.5	0.179	ND
20% DOaG liposomes	Ethanol injection		± 107.5	0.181	ND
30% DOaG liposomes	Ethanol injection		± 136.5	0.281	ND
PAP3 liposomes (50% DOaG)	Extrusion	Day 0	± 142.2	0.123	-6.1*
		Day 5	±157.5	0.225	ND
	Ethanol injection		± 123.0	0.218	-11.2*
PAP3 (*formulated in PBS)*	Extrusion		± 249.1	0.495	ND
PAP3 (*formulated in 10mM Tris pH= 7.4)*	Extrusion		± 124.8	0.218	ND
DSPC:DOaG:IKS02 (45:50:5)	Extrusion		± 129.4	0.163	ND
DSPC:DOG (50:50)	Extrusion		± 161.7	0.318	-7.2
DOPC:DOaG (50:50)	Ethanol injection		± 200.2	0.141	ND
PAP3 liposomes:DSPE-PEG (5 %)	Extrusion		± 113.1	0.060	ND
DSPC:DOaG:NOTA (49.9:49.9:0.2)	Ethanol injection		± 151.3	0.207	ND
DSPC:DOaG:NOTA (49.9:49.9:0.2) *after labeling with Cu^{2+} (cold)*	Ethanol injection		± 260.8	0.231	-8.7
DSPC:DOaG:NOTA (49.9:49.9:0.2) *radiolabeled with $^{64}Cu^{2+}$ just before administration in mice*	Ethanol injection		± 152.2	0.220	ND
DSPC:DOaG:DOPE-pHrodo:DOPE-NBD (49.5:49.5:0.5:0.5)	Extrusion		± 126.2	0.227	ND

* Addition of NaCl for surface charge measurement increases the PAP3 liposome size and PDI (180.8 nm, 0.8 PDI). ND: Not determined.

2.6 References

1. Feingold, K. R.; Grunfeld, C. Introduction to Lipids and Lipoproteins. *Endotext* **2021**.
2. Akinc, A.; Maier, M. A.; Manoharan, M.; Fitzgerald, K.; Jayaraman, M.; Barros, S.; Ansell, S.; Du, X.; Hope, M. J.; Madden, T. D.; Mui, B. L.; Semple, S. C.; Tam, Y. K.; Ciufolini, M.; Witzigmann, D.; Kulkarni, J. A.; van der Meel, R.; Cullis, P. R. The Onpattro Story and the Clinical Translation of Nanomedicines Containing Nucleic Acid-Based Drugs. *Nat Nanotechnol* **2019**, *14* (12), 1084–1087.
3. Akinc, A.; Querbes, W.; De, S.; Qin, J.; Frank-Kamenetsky, M.; Jayaprakash, K. N.; Jayaraman, M.; Rajeev, K. G.; Cantley, W. L.; Dorkin, J. R.; Butler, J. S.; Qin, L.; Racie, T.; Sprague, A.; Fava, E.; Zeigerer, A.; Hope, M. J.; Zerial, M.; Sah, D. W.; Fitzgerald, K.; Tracy, M. A.; Manoharan, M.; Koteliansky, V.; Fougerolles, A. De; Maier, M. A. Targeted Delivery of RNAi Therapeutics with Endogenous and Exogenous Ligand-Based Mechanisms. *Mol Ther* **2010**, *18* (7), 1357–1364.
4. Schrijver, D. P.; de Dreu, A.; Hofstraat, S. R. J.; Kluza, E.; Zwolsman, R.; Deckers, J.; Anbergen, T.; de Bruin, K.; Trines, M. M.; Nugraha, E. G.; Ummels, F.; Röring, R. J.; Beldman, T. J.; Teunissen, A. J. P.; Fayad, Z. A.; van der Meel, R.; Mulder, W. J. M. Nanoengineering Apolipoprotein A1-Based Immunotherapeutics. *Adv Ther* **2021**, *4* (8), 2100083.
5. Wolfrum, C.; Shi, S.; Jayaprakash, K. N.; Jayaraman, M.; Wang, G.; Pandey, R. K.; Rajeev, K. G.; Nakayama, T.; Charrise, K.; Ndungo, E. M.; Zimmermann, T.; Koteliansky, V.; Manoharan, M.; Stoffel, M. Mechanisms and Optimization of in vivo Delivery of Lipophilic siRNAs. *Nat Biotechnol* **2007**, *25* (10), 1149–1157.
6. Ference, B. A.; Ginsberg, H. N.; Graham, I.; Ray, K. K.; Packard, C. J.; Bruckert, E.; Hegele, R. A.; Krauss, R. M.; Raal, F. J.; Schunkert, H.; Watt, G. F.; Borén, J.; Fazio, S.; Horton, J. D.; Masana, L.; Nicholls, S. J.; Nordestgaard, B. G.; Van De Sluis, B.; Taskinen, M. R.; Tokgözoğlu, L.; Landmesser, U.; Laufs, U.; Wiklund, O.; Stock, J. K.; Chapman, M. J.; Catapano, A. L. Low-Density Lipoproteins Cause Atherosclerotic Cardiovascular Disease. Evidence from Genetic, Epidemiologic, and Clinical Studies. A Consensus Statement from the European Atherosclerosis Society Consensus Panel. *Eur Heart J* **2017**, *38* (32), 2459–2472.
7. Goldstein, J. L.; Brown, M. S. A Century of Cholesterol and Coronaries: From Plaques to Genes to Statins. *Cell* **2015**, *161* (1), 161–172.

8. Fielding, C. J.; Fieldinst, P. E. Molecular Physiology of Reverse Cholesterol Transport. *J Lipid Res* **1995**, *36*, 211–228.
9. Allan, C. M.; Fidge, N. H.; Morrison, J. R.; Kanellos, J. Monoclonal Antibodies to Human Apolipoprotein AI: Probing the Putative Receptor Binding Domain of Apolipoprotein AI. *Biochem J* **1993**, *290*, 449–455.
10. Vadiveloo, P. K.; Allan, C. M.; Murray, B. J.; Fidge, N. H. Interaction of Apolipoprotein AII with the Putative High-Density Lipoprotein Receptor. *Biochemistry* **1993**, *32* (36), 9480–9485.
11. Hussain, M. M.; Strickland, D. K.; Bakillah, A. The Mammalian Low-Density Lipoprotein Receptor Family. *Annu Rev Nutr* **1999**, *19*, 141–172.
12. Shen, Y.; Lookene, A.; Zhang, L.; Olivecrona, G. Site-Directed Mutagenesis of Apolipoprotein CII to Probe the Role of Its Secondary Structure for Activation of Lipoprotein Lipase. *J Biol Chem* **2010**, *285* (10), 7484–7492.
13. Amar, M. J. A.; Sakurai, T.; Sakurai-Ikuta, A.; Sviridov, D.; Freeman, L.; Ahsan, L.; Remaley, A. T. A Novel Apolipoprotein C-II Mimetic Peptide That Activates Lipoprotein Lipase and Decreases Serum Triglycerides in Apolipoprotein E-Knockout Mice. *J Pharmacol Exp Ther* **2015**, *352* (2), 227–235.
14. Saito, H.; Lund-Katz, S.; Phillips, M. C. Contributions of Domain Structure and Lipid Interaction to the Functionality of Exchangeable Human Apolipoproteins. *Prog Lipid Res* **2004**, *43* (4), 350–380.
15. Xu, S.; Laccotripe, M.; Huang, X.; Rigotti, A.; Zannis, V. I.; Krieger, M. Apolipoproteins of HDL Can Directly Mediate Binding to the Scavenger Receptor SR-BI, an HDL Receptor That Mediates Selective Lipid Uptake. *J. Lipid Res* **1997**, *3*, 1289–1298.
16. Williams, D. L.; De La Llera-Moya, M.; Thuahnai, S. T.; Lund-Katz, S.; Connelly, M. A.; Azhartt, S.; Anantharamaiah, G. M.; Phillips, M. C. Binding and Cross-Linking Studies Show That Scavenger Receptor BI Interacts with Multiple Sites in Apolipoprotein A-I and Identify the Class A Amphipathic Alpha-Helix as a Recognition Motif. *J Biol Chem* **2000**, *275* (25), 18897–18904.
17. Thuahnai, S. T.; Lund-Katz, S.; Anantharamaiah, G. M.; Williams, D. L.; Phillips, M. C. A Quantitative Analysis of Apolipoprotein Binding to SR-BI: Multiple Binding Sites for Lipid-Free and Lipid-Associated Apolipoproteins. *J Lipid Res* **2003**, *44* (6), 1132–1142.
18. Chroni, A.; Liu, T.; Gorshkova, I.; Kan, H. Y.; Uehara, Y.; Von Eckardstein, A.; Zannis, V. I. The Central Helices of ApoA-I Can Promote ATP-Binding Cassette Transporter A1 (ABCA1)-Mediated Lipid Efflux. Amino Acid Residues 220-231 of

the Wild-Type ApoA-I Are Required for Lipid Efflux in vitro and High Density Lipoprotein Formation in vivo. *J Biol Chem* **2003**, *278* (9), 6719–6730.

19. Wang, N.; Silver, D. L.; Costet, P.; Tall, A. R. Specific Binding of ApoA-I, Enhanced Cholesterol Efflux, and Altered Plasma Membrane Morphology in Cells Expressing ABC1. *J Biol Chem* **2000**, *275* (42), 33053–33058.
20. Denis, M.; Haidar, B.; Marcil, M.; Bouvier, M.; Krimbou, L.; Genest, J. Molecular and Cellular Physiology of Apolipoprotein A-I Lipidation by the ATP-Binding Cassette Transporter A1 (ABCA1). *J Biol Chem* **2004**, *279* (9), 7384–7394.
21. Jaye, M.; Lynch, K. J.; Krawiec, J.; Marchadier, D.; Maugeais, C.; Doan, K.; South, V.; Amin, D.; Perrone, M.; Rader, D. J. A Novel Endothelial-Derived Lipase That Modulates HDL Metabolism. *Nat Genet* **1999**, *21* (4), 424–428.
22. Fuki, I. V.; Blanchard, N.; Jin, W.; Marchadier, D. H. L.; Millar, J. S.; Glick, J. M.; Rader, D. J. Endogenously Produced Endothelial Lipase Enhances Binding and Cellular Processing of Plasma Lipoproteins via Heparan Sulfate Proteoglycan-Mediated Pathway. *J Biol Chem* **2003**, *278* (36), 34331–34338.
23. Mead, J. R.; Irvine, S. A.; Ramji, D. P. Lipoprotein Lipase: Structure, Function, Regulation, and Role in Disease. *J Mol Med* **2002**, *80* (12), 753–769.
24. Connelly, P. W. The Role of Hepatic Lipase in Lipoprotein Metabolism. *Clin Chim Acta* **1999**, *286* (1–2), 243–255.
25. Hirata, K. I.; Dichek, H. L.; Cioffi, J. A.; Choi, S. Y.; Leeper, N. J.; Quintana, L.; Kronmal, G. S.; Cooper, A. D.; Quertermous, T. Cloning of a Unique Lipase from Endothelial Cells Extends the Lipase Gene Family. *J Biol Chem* **1999**, *274* (20), 14170–14175.
26. Santamarina-Fojo, S.; Dugi, K. A. Structure, Function and Role of Lipoprotein Lipase in Lipoprotein Metabolism. *Curr Opin Lipidol* **1994**, *5* (2), 117–125.
27. Landin, B.; Nilsson, Å. Metabolism of Chylomicron Phosphatidylethanolamine in the Rat. *Biochim Biophys Acta* **1984**, *793* (1), 105–113.
28. Dugi, K. A.; Dichek, H. L.; Santamarina-Fojo, S. Human Hepatic and Lipoprotein Lipase: The Loop Covering the Catalytic Site Mediates Lipase Substrate Specificity. *J Biol Chem* **1995**, *270* (43), 25396–25401.
29. McCoy, M. G.; Sun, G. S.; Marchadier, D.; Maugeais, C.; Glick, J. M.; Rader, D. J. Characterization of the Lipolytic Activity of Endothelial Lipase. *J Lipid Res* **2002**, *43* (6), 921–929.
30. Yu, J. E.; Han, S. Y.; Wolfson, B.; Zhou, Q. The Role of Endothelial Lipase in Lipid Metabolism, Inflammation, and Cancer. *Histol Histopathol* **2018**, *33* (1), 1–10.

31. Ishida, T.; Choi, S.; Kundu, R. K.; Hirata, K. ichi; Rubin, E. M.; Cooper, A. D.; Quertermous, T. Endothelial Lipase Is a Major Determinant of HDL Level. *J Clin Invest* **2003**, *111* (3), 347–355.
32. Paradis, M. E.; Lamarche, B. Endothelial Lipase: Its Role in Cardiovascular Disease. *Can J Cardiol* **2006**, *22*, 31B-34B.
33. Jin, W.; Millar, J. S.; Broedl, U.; Glick, J. M.; Rader, D. J. Inhibition of Endothelial Lipase Causes Increased HDL Cholesterol Levels in vivo. *J Clin Invest* **2003**, *111* (3), 357–362.
34. Strauss, J. G.; Zimmermann, R.; Hrzenjak, A.; Zhou, Y.; Kratky, D.; Levak-Frank, S.; Kostner, G. M.; Zechner, R.; Frank, S. Endothelial Cell-Derived Lipase Mediates Uptake and Binding of High-Density Lipoprotein (HDL) Particles and the Selective Uptake of HDL-Associated Cholesterol Esters Independent of Its Enzymic Activity. *Biochem J* **2002**, *368* (Pt 1), 69–79.
35. Merkel, M.; Kako, Y.; Radner, H.; Cho, I. S.; Ramasamy, R.; Brunzell, J. D.; Goldberg, I. J.; Breslow, J. L. Catalytically Inactive Lipoprotein Lipase Expression in Muscle of Transgenic Mice Increases Very Low Density Lipoprotein Uptake: Direct Evidence That Lipoprotein Lipase Bridging Occurs in vivo. *PNAS* **1998**, *95* (23), 13841–13846.
36. Sieber, S.; Grossen, P.; Detampel, P.; Siegfried, S.; Witzigmann, D.; Huwyler, J. Zebrafish as an Early Stage Screening Tool to Study the Systemic Circulation of Nanoparticulate Drug Delivery Systems in vivo. *J Control Release* **2017**, *264*, 180–191.
37. Arias-Alpizar, G.; Kong, L.; Vlieg, R. C.; Rabe, A.; Papadopoulou, P.; Meijer, M. S.; Bonnet, S.; Vogel, S.; van Noort, J.; Kros, A.; Campbell, F. Light-Triggered Switching of Liposome Surface Charge Directs Delivery of Membrane Impermeable Payloads in vivo. *Nat Commun* **2020**, *11*, 3638.
38. Campbell, F.; Bos, F. L.; Sieber, S.; Arias-Alpizar, G.; Koch, B. E.; Huwyler, J.; Kros, A.; Bussmann, J. Directing Nanoparticle Biodistribution through Evasion and Exploitation of Stab2-Dependent Nanoparticle Uptake. *ACS Nano* **2018**, *12* (3), 2138–2150.
39. Arias-Alpizar, G.; Koch, B.; Hamelmann, N. M.; Neustrup, M. A.; Paulusse, J. M. J.; Jiskoot, W.; Kros, A.; Bussmann, J. Stabilin-1 Is Required for the Endothelial Clearance of Small Anionic Nanoparticles. *Nanomedicine* **2021**, *34*, 102395.
40. Hayashi, Y.; Takamiya, M.; Jensen, P. B.; Ojea-Jiménez, I.; Claude, H.; Antony, C.; Kjaer-Sorensen, K.; Grabher, C.; Boesen, T.; Gilliland, D.; Oxvig, C.; Strähle, U.; Weiss, C. Differential Nanoparticle Sequestration by Macrophages and Scavenger

Endothelial Cells Visualized in vivo in Real-Time and at Ultrastructural Resolution. *ACS Nano* **2020**, *14* (2), 1665–1681.

41. Quiñonez-Silvero, C.; Hübner, K.; Herzog, W. Development of the Brain Vasculature and the Blood-Brain Barrier in Zebrafish. *Dev Biol* **2020**, *457* (2), 181–190.
42. Van Leeuwen, L. M.; Evans, R. J.; Jim, K. K.; Verboom, T.; Fang, X.; Bojarczuk, A.; Malicki, J.; Johnston, S. A.; van der Sar, A. M. A Transgenic Zebrafish Model for the in Vivo Study of the Blood and Choroid Plexus Brain Barriers Using Claudin 5. *Biol Open* **2018**, *7* (2), bio.030494.
43. Ulrich, F.; Ma, L. H.; Baker, R. G.; Torres-Vázquez, J. Neurovascular Development in the Embryonic Zebrafish Hindbrain. *Dev Biol* **2011**, *357* (1), 134–151.
44. Zhang, J.; Liss, M.; Wolburg, H.; Blasig, I. E.; Abdelilah-Seyfried, S. Involvement of Claudins in Zebrafish Brain Ventricle Morphogenesis. *Ann N Y Acad Sci* **2012**, *1257* (1), 193–198.
45. Zhang, J.; Piontek, J.; Wolburg, H.; Piehl, C.; Liss, M.; Otten, C.; Christ, A.; Willnow, T. E.; Blasig, I. E.; Abdelilah-Seyfried, S. Establishment of a Neuroepithelial Barrier by Claudin5a Is Essential for Zebrafish Brain Ventricular Lumen Expansion. *PNAS* **2010**, *107* (4), 1425–1430.
46. Ando, K.; Fukuhara, S.; Izumi, N.; Nakajima, H.; Fukui, H.; Kelsh, R. N.; Mochizuki, N. Clarification of Mural Cell Coverage of Vascular Endothelial Cells by Live Imaging of Zebrafish. *Development* **2016**, *143* (8), 1328–1339.
47. Lyons, D. A.; Talbot, W. S. Glial Cell Development and Function in Zebrafish. *Cold Spring Harb perspect biol* **2014**, *7* (2), a020586.
48. Umans, R. A.; Henson, H. E.; Mu, F.; Parupalli, C.; Ju, B.; Peters, J. L.; Lanham, K. A.; Plavicki, J. S.; Taylor, M. R. CNS Angiogenesis and Barriergenesis Occur Simultaneously. *Dev Biol* **2017**, *425* (2), 101–108.
49. O'Brown, N. M.; Megason, S. G.; Chenghua, G. Suppression of Transcytosis Regulates Zebrafish Blood-Brain Barrier Function. *Elife* **2019**, *8*, e47326.
50. Isogai, S.; Horiguchi, M.; Weinstein, B. M. The Vascular Anatomy of the Developing Zebrafish: An Atlas of Embryonic and Early Larval Development. *Dev Biol* **2001**, *230* (2), 278–301.
51. Moradi, M. A.; Bomans, P. H. H.; Jackson, A. W.; van Herk, A. M.; Heuts, J. P. A. A Quantitative CryoTEM Study on Crosslinked Nanocapsule Morphology in RAFT-Based Vesicle Polymerization. *Eur Polym J* **2018**, *108*, 329–336.

52. Moradi, M. A.; Tempelaar, S.; Van Herk, A. M.; Heuts, J. P. A. Morphology Control of Liposome - RAFT Oligomer Precursors to Complex Polymer Nanostructures. *Macromolecules* **2019**, *52* (24), 9476–9483.
53. Wu, Y.; Manna, S.; Petrochenko, P.; Koo, B.; Chen, L.; Xu, X.; Choi, S.; Kozak, D.; Zheng, J. Coexistence of Oil Droplets and Lipid Vesicles in Propofol Drug Products. *Int J Pharm* **2020**, *577*, 118998.
54. Leung, A. K. K.; Tam, Y. Y. C.; Chen, S.; Hafez, I. M.; Cullis, P. R. Microfluidic Mixing: A General Method for Encapsulating Macromolecules in Lipid Nanoparticle Systems. *J Phys Chem B* **2015**, *119* (28), 8698–8706.
55. Brader, M. L.; Williams, S. J.; Banks, J. M.; Hui, W. H.; Hong Zhou, Z.; Jin, L. Encapsulation State of Messenger RNA inside Lipid Nanoparticles. *Biophysj* **2021**, *120*, 2766–2770.
56. De Boeck, H.; Zidovetzki, R. Effects of Diacylglycerols on the Structure of Phosphatidylcholine Bilayers: A 2H and 31P NMR Study. *Biochemistry* **1989**, *28* (18), 7439–7446.
57. Goldberg, E. M.; Lester, D. S.; Borchardt, D. B.; Zidovetzki, R. Effects of Diacylglycerols and Ca2+ on Structure of Phosphatidylcholine/Phosphatidylserine Bilayers. *Biophys J* **1994**, *66*, 382–393.
58. Jiménez-Monreal, A. M.; Villalaín, J.; Aranda, F. J.; Gómez-Fernández, J. C. The Phase Behavior of Aqueous Dispersions of Unsaturated Mixtures of Diacylglycerols and Phospholipids. *Biochim Biophys Acta* **1998**, *1373* (1), 209–219.
59. Goñi, F. M.; Alonso, A. Structure and Functional Properties of Diacylglycerols in Membranes. *Prog Lipid Res* **1999**, *38* (1), 1–48.
60. Szule, J. A.; Fuller, N. L.; Peter Rand, R. The Effects of Acyl Chain Length and Saturation of Diacylglycerols and Phosphatidylcholines on Membrane Monolayer Curvature. *Biophys J* **2002**, *83* (2), 977–984.
61. Campomanes, P.; Zoni, V.; Vanni, S. Local Accumulation of Diacylglycerol Alters Membrane Properties Nonlinearly Due to Its Transbilayer Activity. *Commun Chem* **2019**, *2* (1), 1–8.
62. Allen, T. M.; Hansen, C.; Martin, F.; Redemann, C.; Yau-Young, A. Liposomes Containing Synthetic Lipid Derivatives of Poly(Ethylene Glycol) Show Prolonged Circulation Half-Lives in vivo. *Biochim Biophys Acta* **1991**, *1066* (1), 29–36.
63. Working, P. K.; Newman, M. S.; Huang, S. K.; Mayhew, E.; Vaage, J.; Lasic, D. D. Pharmacokinetics, Biodistribution and Therapeutic Efficacy of Doxorubicin Encapsulated in Stealth® Liposomes (Doxil®). *J Liposome Res* **2008**, *4* (1), 667–687.

64. Otis, J. P.; Zeituni, E. M.; Thierer, J. H.; Anderson, J. L.; Brown, A. C.; Boehm, E. D.; Cerchione, D. M.; Ceasrine, A. M.; Avraham-Davidi, I.; Tempelhof, H.; Yaniv, K.; Farber, S. A. Zebrafish as a Model for Apolipoprotein Biology: Comprehensive Expression Analysis and a Role for ApoA-IV in Regulating Food Intake. *Dis Model Mech* **2015**, *8* (3), 295–309.

65. Miyares, R. L.; De Rezende, V. B.; Farber, S. A. Zebrafish Yolk Lipid Processing: A Tractable Tool for the Study of Vertebrate Lipid Transport and Metabolism. *Dis Model Mech* **2014**, *7* (7), 915–927.

66. Kim, J. Y.; Seo, J.; Cho, K. H. Aspartame-Fed Zebrafish Exhibit Acute Deaths with Swimming Defects and Saccharin-Fed Zebrafish Have Elevation of Cholesteryl Ester Transfer Protein Activity in Hypercholesterolemia. *Food Chem Toxicol* **2011**, *49* (11), 2899–2905.

67. Song, Y.; Cone, R. D. Creation of a Genetic Model of Obesity in a Teleost. *FASEB journal* **2007**, *21* (9), 2042–2049.

68. Nishio, S. I.; Gibert, Y.; Bernard, L.; Brunet, F.; Triqueneaux, G.; Laudet, V. Adiponectin and Adiponectin Receptor Genes Are Coexpressed during Zebrafish Embryogenesis and Regulated by Food Deprivation. *Dev Dyn* **2008**, *237* (6), 1682–1690.

69. Anderson, J. L.; Carten, J. D.; Farber, S. A. Zebrafish Lipid Metabolism: From Mediating Early Patterning to the Metabolism of Dietary Fat and Cholesterol. *Methods Cell Biol* **2011**, *101*, 111–141.

70. Liu, C.; Gates, K. P.; Fang, L.; Amar, M. J.; Schneider, D. A.; Geng, H.; Huang, W.; Kim, J.; Pattison, J.; Zhang, J.; Witztum, J. L.; Remaley, A. T.; Dong, P. D.; Miller, Y. I. Apoc2 Loss-of-Function Zebrafish Mutant as a Genetic Model of Hyperlipidemia. *Dis Model Mech* **2015**, *8* (8), 989–998.

71. Pattipeiluhu, R.; Crielaard, S.; Klein-Schiphorst, I.; Florea, B. I.; Kros, A.; Campbell, F. Unbiased Identification of the Liposome Protein Corona Using Photoaffinity-Based Chemoproteomics. *ACS Cent Sci* **2020**, *6* (4), 535–545.

72. Li, C.; Tan, X. F.; Lim, T. K.; Lin, Q.; Gong, Z. Comprehensive and Quantitative Proteomic Analyses of Zebrafish Plasma Reveals Conserved Protein Profiles between Genders and between Zebrafish and Human. *Sci Rep* **2016**, *6*, 24329.

73. Muller, D. P. R.; Gamlen, T. R. The Activity of Hepatic Lipase and Lipoprotein Lipase in Glycogen Storage Disease: Evidence for a Circulating Inhibitor of Postheparin Lipolytic Activity. *Pediatr Res* **1984**, *18* (9), 881–885.

74. Ori, A.; Wilkinson, M. C.; Fernig, D. G. A Systems Biology Approach for the Investigation of the Heparin/Heparan Sulfate Interactome. *J Biol Chem* **2011**, *286* (22), 19892–19904.

75. Sun, S.; Dean, R.; Jia, Q.; Zenova, A.; Zhong, J.; Grayson, C.; Xie, C.; Lindgren, A.; Samra, P.; Sojo, L.; Van Heek, M.; Lin, L.; Percival, D.; Fu, J. M.; Winther, M. D.; Zhang, Z. Discovery of XEN445: A Potent and Selective Endothelial Lipase Inhibitor Raises Plasma HDL-Cholesterol Concentration in Mice. *Bioorg Med Chem* **2013**, *21* (24), 7724–7734.

76. Lo, P. K.; Yao, Y.; Zhou, Q. Inhibition of LIPG Phospholipase Activity Suppresses Tumor Formation of Human Basal-like Triple-Negative Breast Cancer. *Sci Rep* **2020**, *10* (1), 8911.

77. Zhang, Y. N.; Poon, W.; Tavares, A. J.; McGilvray, I. D.; Chan, W. C. W. Nanoparticle-Liver Interactions: Cellular Uptake and Hepatobiliary Elimination. *J Control Release* **2016**, *240*, 332–348.

78. Wilhelm, S.; Tavares, A. J.; Dai, Q.; Ohta, S.; Audet, J.; Dvorak, H. F.; Chan, W. C. W. Analysis of Nanoparticle Delivery to Tumours. *Nat Rev Mater* **2016**, *1* (5), 1–12.

79. Kuai, R.; Subramanian, C.; White, P. T.; Timmermann, B. N.; Moon, J. J.; Cohen, M. S.; Schwendeman, A. Synthetic High-Density Lipoprotein Nanodisks for Targeted Withalongolide Delivery to Adrenocortical Carcinoma. *Int J Nanomedicine* **2017**, *12*, 6581–6594.

80. Lameijer, M.; Binderup, T.; Van Leent, M. M. T.; Senders, M. L.; Fay, F.; Malkus, J.; Sanchez-Gaytan, B. L.; Teunissen, A. J. P.; Karakatsanis, N.; Robson, P.; Zhou, X.; Ye, Y.; Wojtkiewicz, G.; Tang, J.; Seijkens, T. T. P.; Kroon, J.; Stroes, E. S. G.; Kjaer, A.; Ochando, J.; Reiner, T.; Pérez-Medina, C.; Calcagno, C.; Fischer, E. A.; Zhang, B.; Temel, R. E.; Swirski, F. K.; Nahrendorf, M.; Fayad, Z. A.; Lutgens, E.; Mulder, W. J. M.; Duivenvoorden, R. Efficacy and Safety Assessment of a TRAF6-Targeted Nanoimmunotherapy in Atherosclerotic Mice and Non-Human Primates. *Nat Biomed Eng* **2018**, *2* (5), 279–292.

81. van Leent, M. M. T.; Meerwaldt, A. E.; Berchouchi, A.; Toner, Y. C.; Burnett, M. E.; Klein, E. D.; Verschuur, A. V. D.; Nauta, S. A.; Munitz, J.; Prévot, G.; van Leeuwen, E. M.; Ordikhani, F.; Mourits, V. P.; Calcagno, C.; Robson, P. M.; Soultanidis, G.; Reiner, T.; Joosten, R. R. M.; Friedrich, H.; Madsen, J. C.; Kluza, E.; van der Meel, R.; Joosten, L. A. B.; Netea, M. G.; Ochando, J.; Fayad, Z. A.; Pérez-Medina, C.; Mulder, W. J. M.; Teunissen, A. J. P. A Modular Approach toward Producing Nanotherapeutics Targeting the Innate Immune System. *Sci Adv* **2021**, *7* (10), eabe7853.

82. Zhu, G.; Mock, J. N.; Aljuffali, I.; Cummings, B. S.; Arnold, R. D. Secretory Phospholipase A_2 Responsive Liposomes. *J Pharm Sci* **2011**, *100* (8), 3146–3159.
83. Sharipov, M.; Tawfik, S. M.; Gerelkhuu, Z.; Huy, B. T.; Lee, Y. I. Phospholipase A2-Responsive Phosphate Micelle-Loaded UCNPs for Bioimaging of Prostate Cancer Cells. *Sci Rep* **2017**, *7* (1), 16073.
84. Gómez-Fernández, J. C.; Corbalán-García, S. Diacylglycerols, Multivalent Membrane Modulators. *Chem Phys Lipids* **2007**, *148* (1), 1–25.
85. Alwarawrah, M.; Dai, J.; Huang, J. Modification of Lipid Bilayer Structure by Diacylglycerol: A Comparative Study of Diacylglycerol and Cholesterol. *J Chem Theory Comput* **2012**, *8* (2), 749–758.
86. Holme, M. N.; Rashid, M. H.; Thomas, M. R.; Barriga, H. M. G.; Herpoldt, K. L.; Heenan, R. K.; Dreiss, C. A.; Bañuelos, J. L.; Xie, H. N.; Yarovsky, I.; Stevens, M. M. Fate of Liposomes in the Presence of Phospholipase C and D: From Atomic to Supramolecular Lipid Arrangement. *ACS Cent Sci* **2018**, *4* (8), 1023–1030.
87. Tacken, P. J.; De Beer, F.; Van Vark, L. C.; Havekes, L. M.; Hofker, M. H.; Van Dijk, K. W. Very-Low-Density Lipoprotein Binding to the Apolipoprotein E Receptor 2 Is Enhanced by Lipoprotein Lipase, and Does Not Require Apolipoprotein E. *Biochem J* **2000**, *347*, 357–361.
88. Thisse, B.; Thisse, C. Fast Release Clones: A High Throughput Expression Analysis. *ZFIN Direct Data Submission* **2004**.
89. Liu, C.; Han, T.; Stachura, D. L.; Wang, H.; Vaisman, B. L.; Kim, J.; Klemke, R. L.; Remaley, A. T.; Rana, T. M.; Traver, D.; Miller, Y. I. Lipoprotein Lipase Regulates Hematopoietic Stem Progenitor Cell Maintenance through DHA Supply. *Nat Commun* **2018**, *9* (1), 1–14.
90. Lindegaard, M. L. S.; Nielsen, J. E.; Hannibal, J.; Nielsen, L. B. Expression of the Endothelial Lipase Gene in Murine Embryos and Reproductive Organs. *J Lipid Res* **2005**, *46* (3), 439–444.
91. Lindegaard, M. L. S.; Olivecrona, G.; Christoffersen, C.; Kratky, D.; Hannibal, J.; Petersen, B. L.; Zechner, R.; Damm, P.; Nielsen, L. B. Endothelial and Lipoprotein Lipases in Human and Mouse Placenta. *J Lipid Res* **2005**, *46* (11), 2339–2346.
92. Sieber, S.; Grossen, P.; Bussmann, J.; Campbell, F.; Kros, A.; Witzigmann, D.; Huwyler, J. Zebrafish as a Preclinical in vivo Screening Model for Nanomedicines. *Adv Drug Deliv Rev* **2019**, *151–152*, 152–168.
93. Kemmer, G. C.; Bogh, S. A.; Urban, M.; Palmgren, M. G.; Vosch, T.; Schiller, J.; Günther Pomorski, T. Lipid-Conjugated Fluorescent PH Sensors for Monitoring PH Changes in Reconstituted Membrane Systems. *Analyst* **2015**, *140* (18), 6313–6320.

94. Kremer, J. R.; Mastronarde, D. N.; McIntosh, J. R. Computer Visualization of Three-Dimensional Image Data Using IMOD. *J Struct Biol* **1996**, *116* (1), 71–76.
95. Jin, S. W.; Beis, D.; Mitchell, T.; Chen, J. N.; Stainier, D. Y. R. Cellular and Molecular Analyses of Vascular Tube and Lumen Formation in Zebrafish. *Development* **2005**, *132* (23), 5199–5209.
96. Ellett, F.; Pase, L.; Hayman, J. W.; Andrianopoulos, A.; Lieschke, G. J. Mpeg1 Promoter Transgenes Direct Macrophage-Lineage Expression in Zebrafish. *Blood* **2011**, *117* (4), e49–e56.
97. Arias-Alpizar, G.; Bussmann, J.; Campbell, F. Zebrafish Embryos as a Predictive Animal Model to Study Nanoparticle Behavior in vivo. *Bio Protoc* **2021**, *11* (19), e4173.
98. Schindelin, J.; Arganda-Carreras, I.; Frise, E.; Kaynig, V.; Longair, M.; Pietzsch, T.; Preibisch, S.; Rueden, C.; Saalfeld, S.; Schmid, B.; Tinevez, J. Y.; White, D. J.; Hartenstein, V.; Eliceiri, K.; Tomancak, P.; Cardona, A. Fiji: An Open-Source Platform for Biological-Image Analysis. *Nat Methods* **2012**, *9* (7), 676–682.
99. Schneider, C. A.; Rasband, W. S.; Eliceiri, K. W. NIH Image to ImageJ: 25 Years of Image Analysis. *Nat Methods* **2012**, *9* (7), 671–675.